Transport in 2D superconducting and metallic systems

A thesis Submitted
in Partial Fulfilment of the Requirements
for the Degree of

MASTER OF SCIENCE

by

Kaling Vikram Singh

HBNI Roll: PHYS11202013023

to the

School of Physical Sciences

National Institute of Science Education and Research

Bhubaneswar

29.04.2025

DECLARATION

I hereby declare that I am the sole author of this thesis in partial fulfillment of the requirements for a postgraduate degree from National Institute of Science Education and Research (NISER). I authorize NISER to lend this thesis to other institutions or individuals for the purpose of scholarly research.

Kaliy Vdigh

Signature of the Student
Date: 22/05/25

The thesis work reported in the thesis entitled Transport in 2D superconducting and metallic systems was carried out under my supervision, in the school of Physical at NISER, Bhubaneswar, India.

K. Senapati 22/05/2025

Signature of the thesis supervisor
School: SPS
Date: 22/05/25

ACKNOWLEDGEMENTS

I am deeply grateful for the support and guidance I have received throughout this research project. The successful completion of this work would not have been possible without the contributions of several remarkable individuals.

First and foremost, I would like to express my heartfelt gratitude to my supervisor, Dr Kartikeswar Senapati. His insightful feedback, discussions and constant encouragement have been the bedrock of this research. I am also immensely thankful to the PhDs, Ms. Debashree and Mr. Biswajit who have been instrumental in my work. Their expertise in handling various equipment and their meticulous instruction have been invaluable. The time and effort they invested in teaching me the intricacies of handling equipments have greatly enhanced the quality of my research. Furthermore, the workshop staff including Mr Basudev, Mr Deepak, Mr Umakant and Mr Sridhar were immensely supportive and helpful in construction of the Glovebox, which was essential for my project.

In conclusion, their contributions have been invaluable and I am deeply grateful for their support and guidance. Without their help, guidance, and time, this work would not have been complete.

ABSTRACT

Two-dimensional (2D) materials have transformed modern condensed matter physics and nanotechnology. These systems offer high tunability in their structures, that allows for various device applications. This thesis focuses on the synthesis, characterisation, and device integration of 2D materials, with a particular emphasis on optimizing fabrication techniques for high-quality heterostructures and investigating their electrical and superconducting properties. Graphene and transition metal dichalcogenides (TMDs) are key systems in 2D research due to their tunable band structures, high spin-orbit coupling, and emergent phenomena such as superconductivity and correlated insulating states (Mott insulators). To achieve reproducible heterostructures, fabrication methods such as mechanical exfoliation and Ar ion DC magnetron sputtering are investigated thoroughly. Mechanical exfoliation produces clean, defect-free flakes, whereas sputtering allows for scalable deposition of 2D layers. The incorporation of these materials into field-effect transistors (FETs) reveals gate-tunable charge transport, with graphene FETs showing Dirac-point manipulation and TMD-based devices showing Ising superconductivity. We also reported Weak localization in exfoliated graphene systems, caused due to strain in lattices. Metal-graphene contact quality is investigated in order to control doping and reduce interfacial resistance, which is critical for device performance.

By bridging synthesis challenges with fundamental property exploration, this thesis advances the practical application of 2D materials in electronic devices while also providing insights into quantum phenomena caused by reduced dimensionality. This work demonstrates reproducible methods for creating high-quality 2D heterostructures and incorporating them into microelectronic devices such as field-effect transistors (FETs) by optimizing fabrication techniques such as mechanical exfoliation, lithographic contact printing, etc. Finally, the findings of this comprehensive investigation contribute to a better understanding of low-dimensional physics and lay the groundwork for the scalable integration of 2D materials into future research.

Contents

List of Figures

Thesis Objectives and Structure

The primary goal of this thesis is to calibrate the 2D exfoliation and fabrication procedure followed by conducting transport measurements in superconducting and metallic systems such as $NbSe_2$, Graphene, etc. This project aims to establish protocols for fabricating modern quantum devices and conduct temperature dependent transport measurements for research and quantum device applications.

The thesis is organized in 4 chapters.

1. Chapter 1 introduces 2D materials, their properties along with some fabrication approaches available in literature. This section also includes the theory on gating, superconductivity and device structures, which are useful in this project.

2. Chapter 2 includes the different methods and techniques used for fabrication of 2D material based heterostructures. It also explains the working of the different techniques used in this project and the improvements made in the fabrication protocols.

3. Chapter 3 conveys the main idea of the project, optimization, fabrication and characterization of 2D material based devices for research. It lays out the ideas, limitations and intricacies of 2D device fabrication, their characterization and finally, some interesting results at the end.

4. Chapter 4 talks about $NbSe_2$ superconducting devices, their corresponding measurements and the limitations. Further, we talk about some precautions while handling devices.

Chapter 1

Introduction

Two-dimensional (2D) materials are composed of a single layer of atoms or molecules, lacking translational symmetry in the out-of-plane direction. The first isolated 2D material, Graphene, was synthesized by Geim and Novoselov in 2004 via mechanical exfoliation [3]. Since then, numerous 2D materials have been synthesized, extensively characterized, and integrated into applications ranging from electronics and optoelectronics to catalysis and energy storage [4–6]. These materials exhibit strong covalent bonding within the plane, while adjacent layers are coupled through weak van der Waals (VdW) interactions. The weak interlayer forces facilitate the vertical stacking of distinct 2D layers, enabling the fabrication of tailored heterostructures with novel functionalities. Various classes of 2D materials have been developed, including carbon-based structures (e.g., graphene), transition metal dichalcogenides (TMDs), and 2D perovskites. The reduced dimensionality and constrained degrees of freedom in these systems allow for precise control over key material parameters such as band structure, carrier mobility, and excitonic properties. 2D materials provide a versatile platform for probing intrinsic physical properties and emergent quantum phenomena [7].

2D systems are interesting owing to their electron confinements in 2D planes, that lead to numerous emergent physics such as superconductivity, magnetism and formation of flat bands that host strong electron-electron correlations due to low bandwidth of the dispersion relation [8]. Further, 2D Moire materials are emerging class of ma-

terials that have monolayers of 2D material stacked together at an angle called twist angle, that leads to emergence of properties such as flat bands, superconductivity in graphene, and exciton in TMDs such as MoS_2 and WSe_2. Such materials are particularly interesting due to their tunability and thin design which can be used in modern devices that require compact sizes and high efficiency [9].

There are two approaches to fabricate 2D materials - the top down and the bottom up approach. The first approach uses a bulk material that is thinned down through exfoliation procedures while the latter approach uses different synthesis procedures such as CVD, PLD, sputtering, etc. for synthesis of 2D materials. The layers in 2D materials are bounded by Van Der Waal's forces (VdW), and can be cleaved by applying forces more than VdW forces. More details on VdW forces is given in appendix 4.1. Top down approaches are generally preferred due to their high quality yield. Exfoliation methods, in particular, are widely used in research to create high-quality, defect-free 2D heterostructures. Despite superior quality, materials synthesized through exfoliation processes are often limited by their small yield and low scalability [10].

1.1 Properties of 2D materials

2D materials host emergent quantum properties on its interface, but also are highly susceptible to degradation which limit their applications to only sophisticated systems. The current research is focused on use of 2D material to study these emergent properties and find ways to integrate these materials in new devices [11]. Most extensively studied and understood 2D material is graphene.

Graphene

Graphene is the first synthesized and most studied 2D material. It is the top layer of graphite, an allotrope of carbon, where atoms arranged in a hexagonal honeycomb lattice with bondlength of 1.45 Å. Graphite is made of graphene sheets stacked together with an interplanar spacing of 3.35 Å. The carbon atoms are held by 3 σ and 1 π bonds where σ bonds result from an overlap of Sp^2 hybrid orbitals, whereas π and π^* (half filled) bonds emerge from tunneling between the protruding p_z orbitals in adjacent atoms. The band structure of graphene allows for various applications in electronics. Graphene, unlike graphite, has linear dispersion relations at the Bruilloin edges and the conduction and the valence bands meet at the Dirac point.

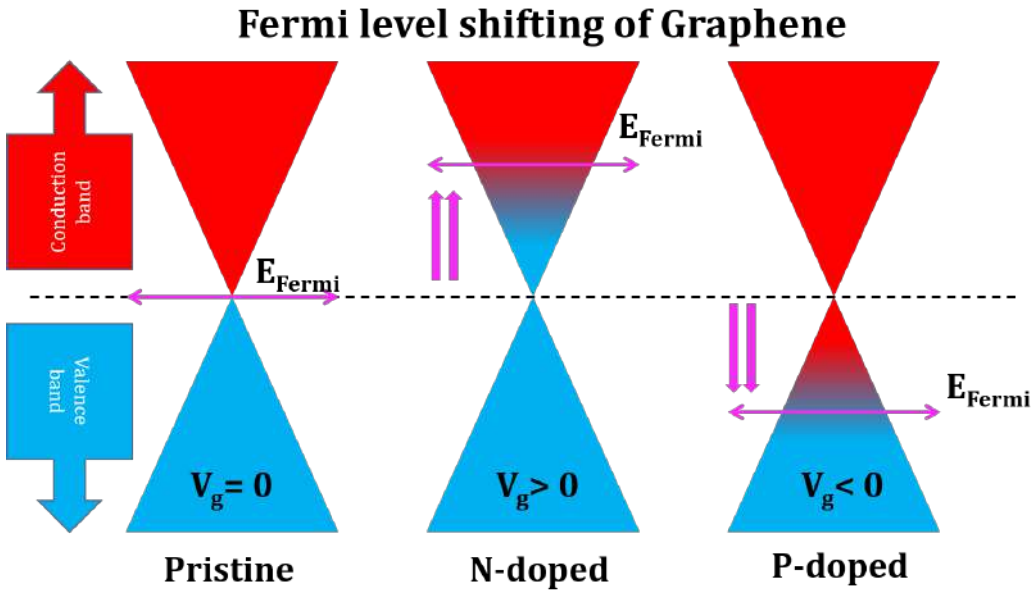

Figure 1.1: Graphene Fermi level tuning

For a pristine graphene, the Fermi level lies at the Dirac point, but shifts into conduction or valence band based on charge doping in the system, as shown in Fig:1.1. The ease of charge doping in these graphene systems makes them highly desirable for applications in transistors and electric devices.

Transition Metal Dichalcogenides (TMDs)

Transition Metal Dichalcogenides (TMDs) are materials that have a general formula MX_2, where M is a transition metal and X is a chalcogen. TMDs have a layered structure, held together by VdW forces and have highly tunable bandgaps. These systems have high charge carrier mobilities and host quasiparticles such as excitons, Polarons, etc. leading to various applications in photonics and sensing. Further, Janus TMDs are a novel class of asymmetric transition metal dichalcogenide (TMD) monolayers that contain an out-of-plane optical dipole and intrinsic piezoelectricity [12]. These characteristics along with structural symmetry results in an amplified Rashba spin-orbit interaction, suggesting that it has a lot of potential for spintronic applications. Bulk TMD have an indirect gap at the Brillouin zone center, while monolayer TMDs have direct band gap at the K points. TMDs such as MoS_2, WSe_2 host excitons and polarons that have potential applications in photonics [13]. Due to heavy transition metals and d orbital electron contribution, TMDs have a strong spin-orbit coupling (SOC). SOC lifts off the spins degeneracy in both conduction and valence bands, splitting the bands between spin up and down states. Using these properties, many new devices showing varied properties can be fabricated.

2D materials can be stacked together to form VdW heterostructures. 2D materials are stacked and held together by van der Waals forces to create van der Waals heterostructures. These pristine layers do not form strong chemical connections with one another because their surfaces are atomically smooth and lack dangling bonds. Stacking is not the same as epitaxial growth, in which layers form direct bonds with the atoms of a substrate. By autonomously developing and then transferring the layers, van der Waals interfaces, allow the assembly of extremely dissimilar materi-

als [7, 14]. These materials are highly tunable, and by applying physical constraints, such as pressure, layer rotation, etc. one can alter the properties of these materials.

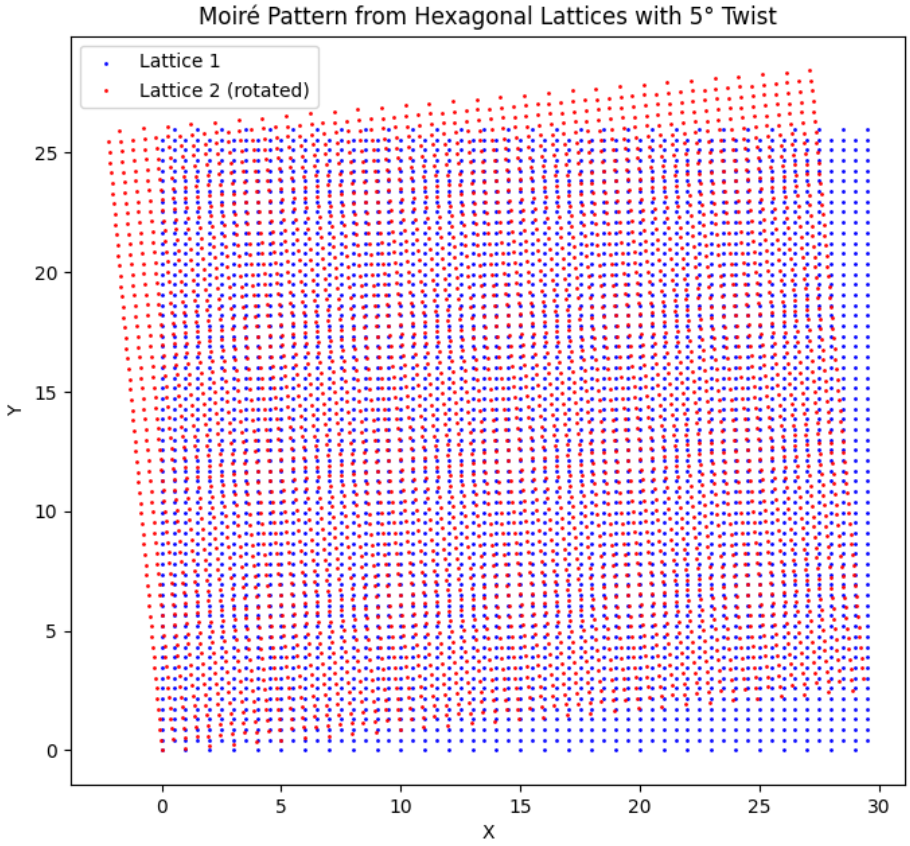

Figure 1.2: Moiré lattice

The electrical characteristics of 2D materials can still be altered by the adjacent layers, even in the presence of relatively weak VdW interactions. For example, charge carrier mobility in a stack of hBN/graphene/hBN is higher than graphene on amorphous silicon dioxide or hung without support. Two or more monolayers of 2D materials can be stacked together at an angle, as shown in Fig: 1.2, creating a new class of materials, called Moiré materials which induce periodicity in the lattice leading to emergent properties such as superconductivity in magic angle twisted graphene or , insulating, or ferromagnetic phases in TMDs [15].

1.2 Fabrication methods

Over time, different top-down and bottom-up approaches for isolating or growing 2D materials have emerged. Research into the synthesis of 2D materials is still quite active, with an emphasis on enhancing material quality, controlling layer thickness, and expanding substrate sizes. Some of the common approaches include chemical vapor deposition (CVD), mechanical exfoliation, liquid phase exfoliation, molecular beam epitaxy, etc. Generally top - down approaches are preferred in research due to high purity of samples obtained through these processes.

1.2.1 Chemical Vapor Deposition (CVD)

CVD utilizes a bottom up approach for 2D material fabrication. It consists of constituent atoms as precursors to synthesize 2D materials at high temperatures through controlled deposition parameters, such as pressure, temperature, flow rates and time of deposition [16]. This method yields lower quality 2D materials compared to traditional technique of mechanical exfoliation, but are used because of their higher yield and ease of operation. Further, the deposition occurs at high temperature, that can lead to lattice relaxation and oxidation causing defects in the fabricated samples. Besides this, the 2D materials synthesized needs to be transferred onto a substrate for device fabrication, which requires highly calibrated methods of chemical or mechanical exfoliation for flake transfer.

1.2.2 Mechanical exfoliation

Mechanical exfoliation is the process of peeling individual layers from a bulk crystal of a layered material. This method takes advantage of the weak VdW forces between layers as well as the strong in-plane bonds that keep each 2D sheet structurally intact.

A scotch tape is pressed onto a crystal and peeled, cleaving few layers of materials onto its adhesive. This is then transferred to substrates for studies. It was first used to separate graphene from graphite and is still a valuable technique for creating high-quality 2D layers in research. However, the exfoliated layers are typically only a few micrometers large, making this method unsuitable for producing materials on large-scale substrates.

1.2.3 Liquid Phase Exfoliation

Another extensively used approach is liquid phase exfoliation (LPE). Unlike mechanical exfoliation, LPE is a solution-based approach for manufacturing large numbers of 2D nanosheets at a low cost. Nonetheless, its application is limited by issues such as poor sample quality and small flake sizes. In a LPE process, bulk crystals are immersed in a predetermined solvent and mechanical forces, such as sonication or shear mixing, are subsequently used to separate the bulk material into distributed 2D nanosheets. The lateral dimensions and thickness of the flakes can be adjusted by varying the sonication and mixing strengths. Achieving an optimum solvent surface tension is critical in LPE for reducing exfoliation energy and stabilizing the nanosheets.

While there are various methods for 2D material fabrication, in this thesis the process of mechanical exfoliation and contact printing using lithography followed by Ar ion DC magnetron sputtering is extensively studied and optimized. This project aims to fabricate micro devices using 2D materials and study their properties, while optimizing the intermediate steps for obtaining reproducible heterostructures. One of the commonly fabricated and used device is a transistor, especially Field effect Transistors, which is a devices that allows current modulation through electronic circuits.

These are used in modern day computer circuits for various gate operations.

1.3 Field Effect Transistors (FET)

Field effect Transistors (FETs) are three terminal devices that use electric fields to manipulate the source - drain current passing through them. These devices have use in many electronic systems such as memory devices, amplifiers, switches, etc. Metal-Oxide-Semiconductor Field-Effect Transistor (MOSFETS) that are used in photo emissions and photo diodes are also based on FETs and are backbone of semiconductor manufacturing industry. A schematic of a FET is shown in Fig:1.3.

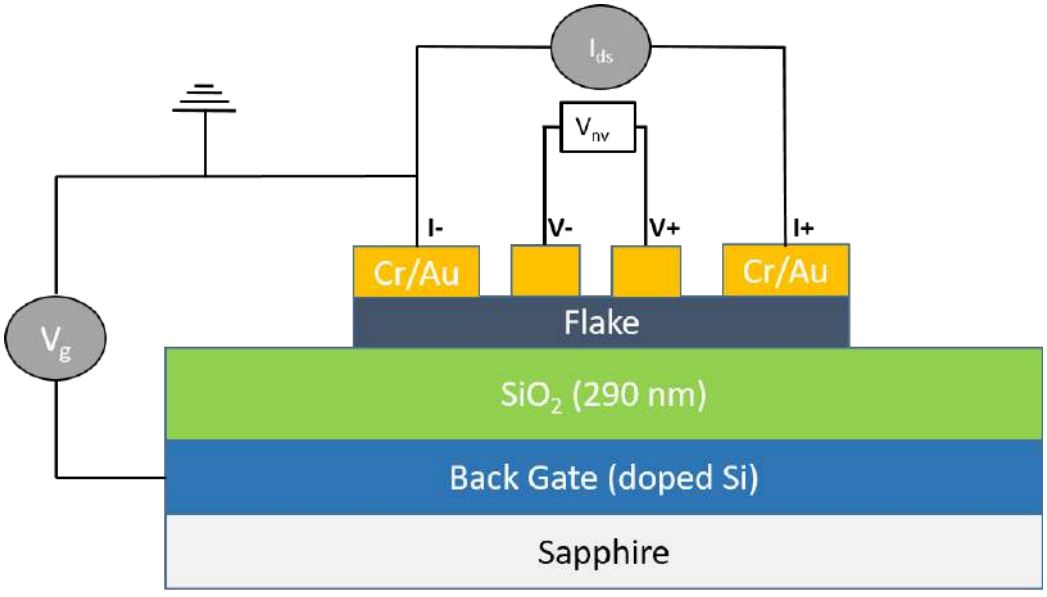

Figure 1.3: Schematics of a FET

The setup consists of a back gate, generally heavily doped Si, followed by a SiO_2 oxide layer, that acts as the dielectric and a capacitor in the circuit and allows for charge accumulation in its edges. Finally, the target channel is placed on top of SiO_2, with source - drain electrodes and gate bias grounding as shown in Fig:1.3. The whole setup is placed on a sapphire substrate to reduce leakage currents to the sample holder.

The source drain bias (V_{ds}) allows for a directional flow of charges, while the gate bias (V_g) accumulates charges, increasing the carrier density and hence the overall current. The charge accumulated is given by:

$$Q_{in} = C_{ox}(V_g - V_{th}) \tag{1.1}$$

where V_{th} is the threshold voltage. In different systems, V_{th} corresponds to different effects, such as for MOSFETs, V_{th} corresponds to contribution from depletion region in pn junctions at the electrodes and in graphene FETs, V_{th} corresponds to the Dirac voltage. Thus, the conduction is minimized when $V_g = V_{th}$ due to the low charge carrier densities. FETs can be fabricated using 2D materials such as Graphene an other TMDs.

1.3.1 Graphene Field Effect Transistors (GFET)

Graphene FETs use graphene as the conduction channel, placed on the SiO_2, as shown in Fig:1.3. The idea of GFETs is based on doping in graphene systems by manipulating the Fermi level through electric gating. This induces holes/electrons in the graphene channel, increasing or decreasing the conductivity based on the doping in the system. A back voltage of $V_g > 0$ induces electrons in the graphene channel, making it N doped while a negative back voltage induces holes, making the graphene P doped. At Dirac point, the charge carrier density is least and we observe highly resistive transport. Using this method, the Fermi level can be shifted to observe strong electron correlations (due to higher charge densities) and manipulate the current in the systems. Gating in graphene can help in achieving quantum hall effects and Shubnikov De Haas oscillations at room temperatures in high fields ($\sim$ 45 T) [17].

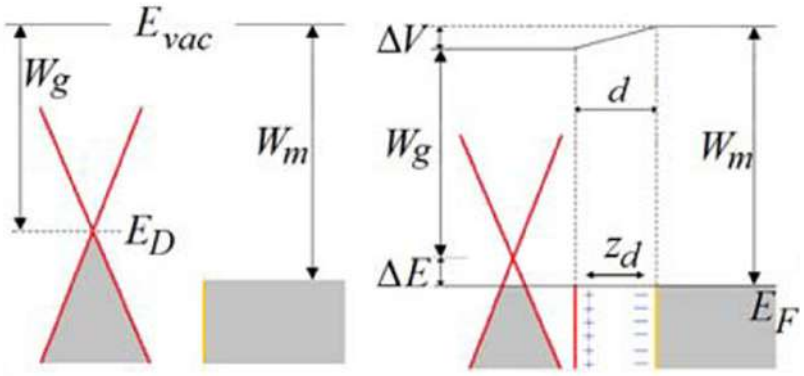

Figure 1.4: Metal - Graphene contact [1]

Interestingly, graphene can be inherently doped through metal deposition through charge transfer in graphene from metal, based on its work function [18], as shown in Fig 1.4. A proper contact to GFET is crucial for device fabrication. If the Fermi level of the metal is higher than graphene, electrons are doped into graphene channel, forming a n-doped graphene, while a lower Fermi level of metal forms a p doped graphene channel due to flow of electrons from graphene to the metal. Following this, one can verify a proper contact between the contacts and the flakes and perform operation using gating. Beyond GFETs, there are TMD based heterostructures that are fabricated to study material properties and understand various coherent phenomena, such as charge density waves (CDW), superconductivity, phase transitions, etc. Superconductivity in particular is very interesting in these systems due to their applications in nano devices, that have uses in fields like single photon emitters, detectors, antennas etc [19, 20].

1.4 Superconductivity in thin films

Superconductivity is the property of certain materials to conduct electricity without any resistance at low temperatures. These materials also show Meissner effect, where the material expels magnetic field and shows perfect diamagnetism. In known sys-

tems, a clean, single step transition in resistance at a fixed temperature is a signature of defect-free superconductor. In a superconductor, the $\vec{K}$ and $-\vec{K}$ momenta electrons are paired, called Cooper Pairs, generally through phonon mediated coupling, forming a Bosonic state [21–23]. All the cooper pairs condense into a single lower energy Bosonic state forming an energy gap in the energy dispersion, as shown in fig 1.5. The superconducting gap can be calculated using the BCS theory (see appendix 4.2) using the obtained T_c and is given by:

$$\Delta(0) = 1.74 K_b T c \tag{1.2}$$

where $\Delta(0)$ is the superconducting gap at T = 0K, K_b is the Boltzmann constant and T_c is the transition temperature. In superconductors, cooper pairs carry electric current and offer no resistance for current flow. If the temperature or the potential applied is high enough, the cooper pair start to scatter from lattices and break, transitioning the superconductor to a normal state. The maximum current that a superconductor can withstand without losing its properties is called critical current (I_c) [24].

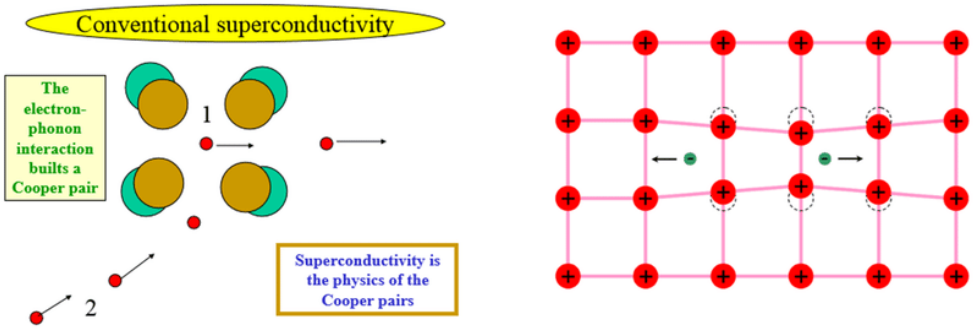

Figure 1.5: Cooper Pair formation [2]

In presence of high magnetic field, a superconductor - normal metal transition is

observed. Type I superconductors have a sharp transition at H_c, when the applied magnetic field leads to spin flipping of the opposite spin electrons, breaking cooper pairs. In type II superconductors, at lower fields upto H_{c1}, the material show perfect diamagnetism. Above H_{c1}, magnetic fields start to penetrate the superconductor forming Abrikosov vortices, where magnetic field penetrates through quantized vortices and is shielded by a loop of supercurrent. Two vortices repel each other and they can be moved inside the material through electric field application. GL theory (see appendix 4.3) explains the phase dynamics of type II superconductors, which are used in most studies.

As the superconductors are thinned, the electron - electron interactions dominate due to lower screening and phonon mediated processes being suppressed. Further, stray magnetic fields and effects from defects dominate in these systems. Thus, thin films show reduction in the transition temperature (T_c) as they are thinned down. In order to miniaturize devices for applications, 2D superconductors are essential, but their fabrication is specifically tough due to defects in these systems. In this work, we fabricate 2D superconducting devices and observe their properties such as CDW formation and transition temperature to verify defect free fabrication. We use $NbSe_2$ flakes for the device fabrication, based on the optimized parameters from Graphene exfoliation.

1.4.1 Niobium Diselenide

Niobium Diselenide ($NbSe_2$) is a transition metal dichalcogenide (TMD) and a superconductor with a bulk transition temperature (T_c) of 7.2 K in the 2H layered form. It also shows a CDW order near 33K. A single layer of $NbSe_2$ consists of a Nb atom sandwiched between 2 Se atoms, arranged in hexagonal structure [25, 26].

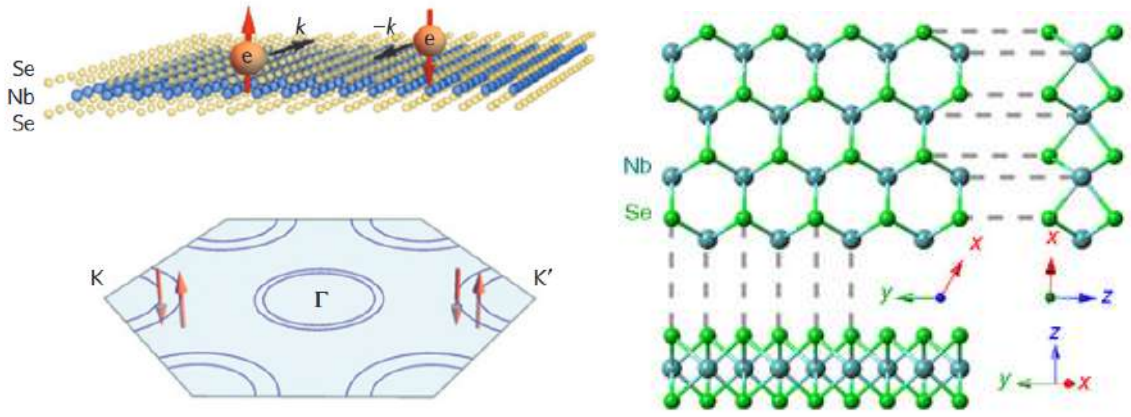

(a) Spin momenta locking in $NbSe_2$ [27] (b) Monolayer $NbSe_2$

Figure 1.6: $NbSe_2$ structure

In 2D limits, the T_c shifts to 2K as the flakes are thinned down to monolayers. $NbSe_2$ flakes experience breaking of out of plane inversion symmetry, causing the spin to be locked in out of plane direction. This is called Ising superconductivity and has peculiar behavior such as having H_{C2}, much higher than the Pauli limit. Thus, many interesting quantum phenomena develop as TMDs such as $NbSe_2$ are thinned down.

The spin-momentum locking protects Cooper pairs from the Zeeman effect when magnetic fields are applied in-plane. For in-plane fields, H_{c2} of $NbSe_2$ significantly exceeds the Pauli paramagnetic limit - the maximum field at which a superconductor can withstand spin-alignment-induced pair-breaking. $NbSe_2$'s enhanced field tolerance makes it suitable for future applications like quantum computing, spintronics, and quantum sensors. Its ability to maintain superconductivity in high magnetic fields makes it an ideal material for topological quantum devices, which require spin texture manipulation and quantum state protection.

CDW order in $NbSe_2$

A Charge Density Wave (CDW) order is a quantum phenomenon that occurs in certain materials, particularly in low-dimensional systems like linear chain compounds and layered crystals. In this state, the electronic charge density is spatially modulated, resulting in a periodic wave-like pattern across the material. This modulation is frequently followed by a distortion of the underlying atomic lattice. Researchers are still debating the origin and mechanisms of the CDW transition, which has attracted special attention [28, 29]. The current understanding of CDW formation in $NbSe_2$ is still unclear. Few theories that explain CDW order include:

Fermi Surface Nesting: At first, it was thought that the main factor influencing CDW formation was Fermi surface nesting. This process facilitates electron-hole pairing and subsequent charge modulation by connecting matched regions of the Fermi surface with a single wave vector. More recent research, however, has questioned whether this explanation is adequate for $NbSe_2$.

Strong electron Phonon coupling: The formation of CDW has been found to be significantly influenced by strong electron-phonon coupling (EPC). According to this mechanism, even in the absence of ideal nesting conditions, the interaction between electrons and lattice vibrations (phonons) is essential for maintaining the CDW state.

Van Hove Singularities: Van Hove singularities (vHs) or saddle points in the electronic band structure has also been suggested as a possible driver for CDW formation. These features can lead to an enhanced density of states (DOS) near the Fermi level, potentially facilitating CDW instability.

Finally, impurities and defects can also lead to formation of a CDW order, but more investigations are required to understand the origin of the CDW order and the co-existence of superconductivity in $NbSe_2$ flakes. In this work, we perform transport measurement in 2D $NbSe_2$ flakes, after optimizing the intermediate steps for transport in Graphene channel. We observe CDW behavior and superconductivity transition in these exfoliated flakes and optimize the parameters for future studies in this field. In this regard, Hall effect is one of the most basic methods to check proper contacts and observing quantum properties.

1.5 Hall effect

Hall effect occurs when a magnetic field is applied perpendicular to a current-carrying conductor, which results in a transverse voltage called the Hall voltage (V_H). The Hall resistance (R_H) is proportional to the material's carrier density n [30]. This relationship allows us to calculate charge carrier density using Hall measurements. R_H is given by:

$$R_H = \frac{V_H}{IB}$$

where, V_H is the Hall voltage,I is applied bias current, and B is the perpendicular magnetic field. In the case of a 2D material like graphene, the Hall resistance is related to the charge carrier density n by the following formula:

$$R_H = \frac{1}{ne}$$

where, n is the 2D carrier density (in carriers per unit area, cm^{-2}), e is the elementary charge ($e = 1.602 \times 10^{-19}$ C). Therefore, the charge carrier density can be calculated

as:

$$n = \frac{1}{R_H e}$$

To experimentally determine the Hall resistance R_H, we measure the Hall voltage V_H and apply a known current I and magnetic field B. The slope of Hall resistance R_H vs. magnetic field B yields the slope S (in units of $\Omega \cdot \mathrm{T}^{-1}$), which can be used to calculate the charge carrier density as:

$$S = \frac{1}{neI} \tag{1.3}$$

Hall effect is a good indicator of ballistic transport and provides a way to confirm ohmic contact to samples [31]. We utilize various approaches in our fabricated devices to study the properties of materials and using them, fabricating quantum devices.

Chapter 2

Experimental Methods

2.1 Exfoliation setup and Procedure

The exfoliation setup consists of an optical microscope, a PID-controlled stage heater with a vacuum suction hole, and a micromanipulator with X, Y, and Z degrees of movement, as shown in fig 2.1a.

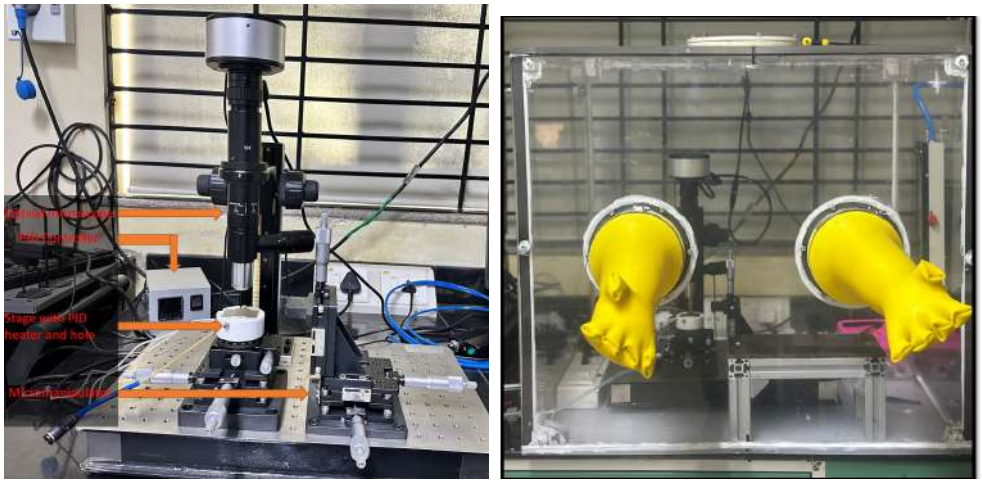

(a) Flake aligner (b) Glovebox

Figure 2.1: Flake aligner and exfoliation setup

A metal glass slide with a 2cm x 2cm slit is mounted in the micromanipulator. The slit is covered using a glass slide using tapes and a adhesive transparent stamp is pasted onto the glass slide (such that the sticky side faces outwards), as shown in fig 2.3. This configuration allows for precise adjustment of the flakes onto the contacts, using the optical microscope that sees through the slit, across the stamps and transparent materials. First, a scotch tape is pressed onto the crystal and gently peeled off, cleaving sample layers onto the tape. This is repeated twice or thrice depending

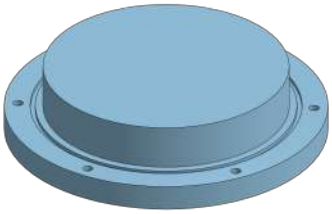

(a) Cap for sample loading

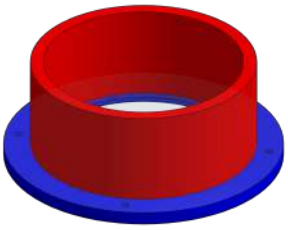

(b) Flanges

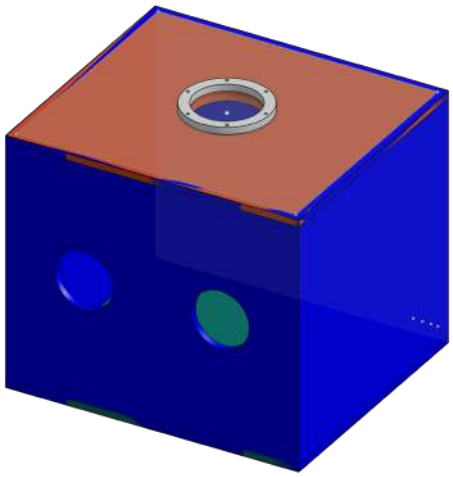

(c) Box design

Figure 2.2: Design for Glove box

on size of the crystal. The tape is then folded onto itself and peeled off repeatedly for 11-12 times until a uniform, shiny and small layers of material is visible as shown in fig 2.4a. The scotch tape obtained after exfoliation must have the following characteristics: It shall be shiny to ensure that the stamp is not in contact with scotch tape which hampers the stamp surface topology. This also ensures, the crystals are not over-exfoliated, causing breaking of the flakes. The flakes should be small in size and uniformly distributed to ensure thin layers are obtained on the PPC stamp with higher probabilities. Large flakes indicate higher thickness and thus cannot be used for 2D studies.

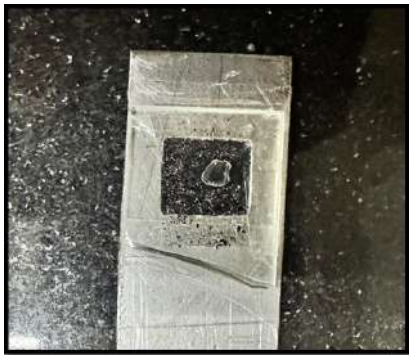

Figure 2.3: Metal slide - PPC assembly

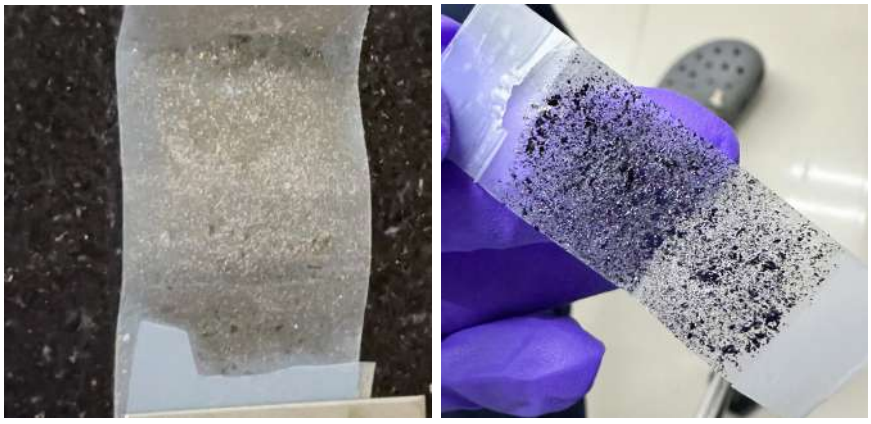

(a) Small and uniform flakes (b) Patchy and large flakes

Figure 2.4: Scotch tape for exfoliation

To improve the protocols, setup was improved by constructing a Glove box, and placing the flake aligner system inside it to ensure oxygen free exfoliation to obtain defect free heterostructures. The images of the updated system is shown in fig: 2.1b. This system prevents sample oxidation during the flake transfer process, which helps in reproduceability of flake heterostructures fabrication.

2.1.1 Viscoelastic Dry Transfer

Viscoelastic dry exfoliation is a method for separating thin layers or monolayers of two-dimensional (2D) materials like graphene, MoS_2, and van der Waals crystals. In this process, a viscoelastic stamp, generally made of Polypropylene Carbonate (PPC)

or PDMS, is used to mechanically exfoliate flakes off a exfoliated scotch tape without the need of solvent.

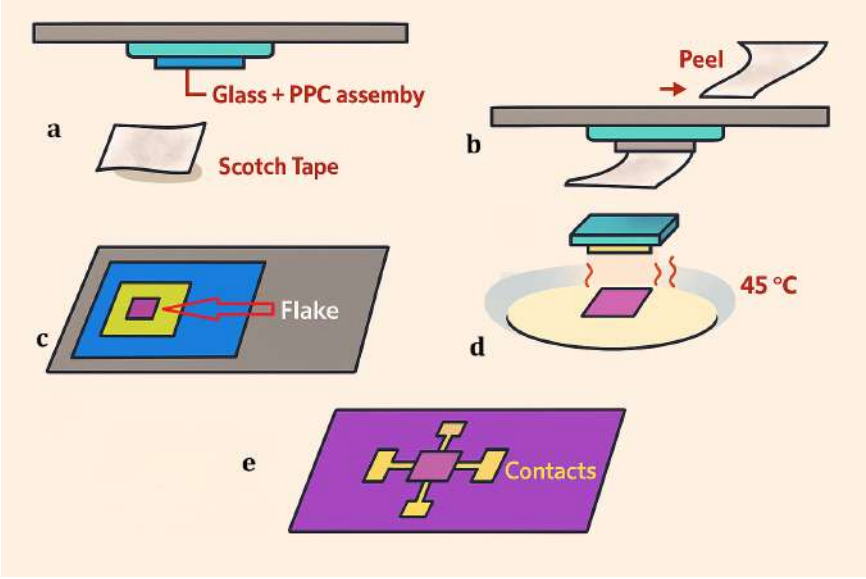

Figure 2.5: Viscoelastic dry exfoliation and transfer (a → e)

The method starts with gently pressing the PPC stamp onto an exfoliated scotch tape, allowing weak van der Waals forces to assist peel off tiny layers when the stamp is pulled back. The angle and speed of peeling is essential for obtaining thin flakes of materials. For example, in graphene, the flakes needs to be pulled parallel to the PPC stamp at very low speeds. In case of $NbSe_2$, relatively faster peeling at a comparatively lower angle is used as $NbSe_2$ has stronger Van Der Waal's interactions between adjacent layers. Beside this, multiple tries may be required to get a basic idea of dry transfer to be able to get reproducibility in the fabrication. These exfoliated flakes stick to the stamp and can be transferred to a desired substrate by aligning and making contact under regulated conditions, such as gentle heating or pressure. The stamps' viscoelastic properties allows conformal contact during exfoliation and controlled release during transfer, resulting in high-quality flake transfer with little contamination. When the sample is ready for transfer, the substrate is heated to

45^{O}C and PPC film is placed onto it. After waiting for 1 minute, PPC stamp is peeled using the Z manipulator of the flake aligner. It was ensured that the vacuum suction is on so as to cleave PPC stamp from the substrate. Peeling the stamp at faster rates increases the risks of flakes damage, unsuccessful transfer and loss of stamp on the substrate. The whole procedure is shown in fig 2.5. This dry technique does not include chemical processing, keeping the structural and electrical integrity of the exfoliated layers and making it ideal for creating clean 2D materials for electronic, optical, or quantum device applications.

2.1.2 Viscoelastic stamp preparation

The Viscoelastic stamp is a 2mm x 2mm, patch of PPC that has glass transition temperature of 45^{0}C and is prepared by dissolving PPC pellets in Anisole (methoxybenzene, 99% pure). A 15% wt/wt (1.5g in 8.631mL Anisole) solution is prepared by first dispersing PPC in Anisole followed by heating on a hot plate with magnetic stirring for minutes at 50^{0}C. The solution is ultrasonicated in between, twice for 10 minutes each to ensure proper dissolution of PPC in Anisole. Next, the solution is transferred to a petridish and kept in a desiccator, followed by degassing for 25 minutes until the bubbles cease to pop. Then solution is then kept on hot plate for 4.5 hours at 60^{0}C to evaporate the Anisole and get a uniform PPC film. The film is allowed to cool for an hour and 2mm x 2mm stamps are cut using a surgical knife for exfoliation process. Anisole is carcinogenic, thus utmost care shall be taken while dealing with PPC film.

2.2 DC magnetron Sputtering

The deposition technique used has a significant impact on the thickness and quality of a thin film. Usually composed of layered materials, thin films are created by applying

several deposition processes to a substrate. Among these, Physical Vapor Deposition (PVD) is a well-known technique that makes it possible to create films with nanoscale thickness. Sputtering is a popular PVD method that is frequently used to deposit thin films of different materials. Sputtering involves accelerating ions toward a target material, resulting in the ejection of atoms or molecules from the target's surface. These expelled species eventually condense on the substrate, forming a thin coating. Sputtering can be divided into two forms based on how the ionized particles are generated: DC (Direct Current) and RF (Radio Frequency). An illustration is shown in Fig. 2.6a.

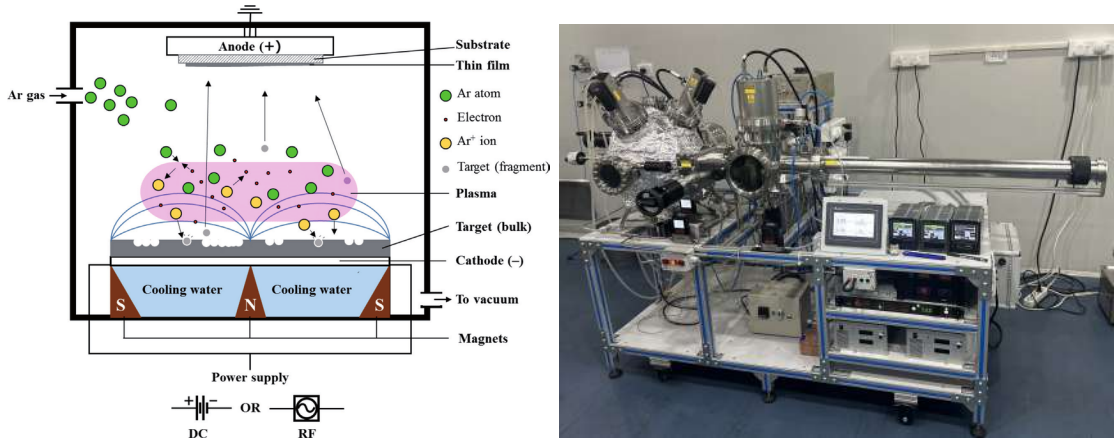

(a) Magnetron Sputtering System [32] (b) Sputtering & Ar^+ ion milling system

Figure 2.6: Magnetron sputtering and ion milling setups

In DC sputtering, a high voltage is applied between the target (cathode) and the substrate (anode), ionizing the inert gas (usually argon) inside the vacuum chamber. The positively charged ions are subsequently propelled towards the negatively charged target. These ions strike the target and eject atoms from its surface, which then settle on the substrate. Plasma creation is a critical phase in the process. It starts when accelerating electrons clash with gas atoms, ionizing them and producing extra free electrons and positive ions. Primary electrons are ejected from the target

by the electric field, whereas secondary electrons are released when ions strike the target. This approach requires high voltage to create thin films, making it less efficient. Thus, we add a magnetic field to the plasma by placing a magnet above the target. The magnetic field causes expelled electrons to follow helical trajectories instead of straight lines. This effect increased electron collisions with gas molecules, leading to a more dense plasma with less power. This process is known as DC magnetron sputtering.

DC magnetron sputtering was used to print contacts onto 2D materials. Several materials and procedures were tried to calibrate the contact printing, after lithography. Two different appraches - the pre patterned and the post patterned approaches were used to fabricate samples and understand the effects of patterning and different metal contacts.

2.3 Ar^+ ion milling

Argon ion (Ar^+) milling is also a physical sputtering technique used for surface modification, cleaning, and accurate material removal. A focused beam of high-energy argon ions is directed toward the sample surface in a high-vacuum environment. As the inert argon ions strike the surface, they transfer momentum to surface atoms via elastic collisions, physically chipping them off without causing chemical reactions. Because argon is chemically inert, this technique maintains the stoichiometry and chemical structure of most materials while allowing for nanometer-scale etching accuracy. Tuning parameters such as ion energy, beam current, incident angle, and milling time control the milling rate and depth respectively. This method is similar to magnetron sputtering but with very high driving potentials and the argon ions

etch away the thin film. The DC Magnetron sputtering and Ar^+ ion milling system used in this project is shown in fig 2.6b. The system allows for insitu milling and sputtering of target materials, which allows for fabrication of low defect devices.

2.4 Photolithography

Patterned thin film deposition can be obtained in two ways: by patterning the substrate with photoresist before deposition, or by depositing the thin film first and then patterning it with photoresist. Both methods rely on lithography techniques for patterning. Photolithography uses a light-sensitive substance called photoresist, which becomes chemically active when exposed to certain light energy and may then be dissolved with a developer solution. The process begins with spin coating, which applies a homogeneous layer of photoresist on the substrate. The resist is then gently baked to eliminate the solvents and solidify it. The coated substrate is next exposed to radiation, which selectively directs light onto the surface - either through a mask in UV lithography or directly via a focused laser in laser lithography. Following exposure, development occurs, during which the exposed or unexposed portions dissolve, depending on whether a positive or negative resist is used. Optimizing spin-coating, exposure, and development settings is critical for producing high-resolution patterns.

If the thin coating is applied prior to lithography, the sample is photoresist-patterned and the unprotected sections are removed using argon ion milling. The photoresist acts as a mask, protecting the underlying film from the plasma when milling. Afterward, the resist is removed with acetone, leaving behind the patterned film. Alternatively, if the photoresist is patterned first and then the thin film is applied, the material coats both the resist and the exposed substrate.

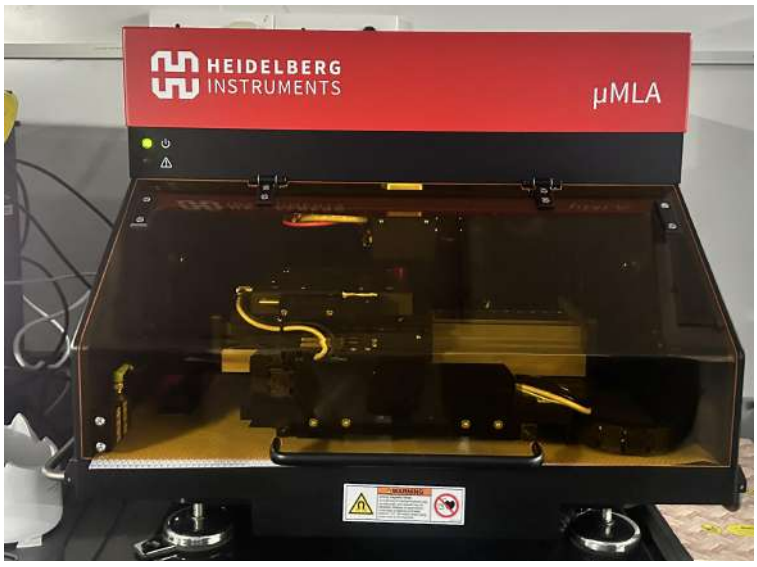

Figure 2.7: Maskless Photolithography system (μMLA)

When the resist is dissolved in acetone, the layer on top is pulled off, revealing a patterned structure. This is referred to as the lift-off procedure. Both procedures yield complementary patterns, and in order to achieve identical designs using either method, a negative approach - such as a negative resist or inverse mask - is required. For our needs, which included developing unique designs, we used Heidelberg's Maskless Laser Lithography system in the cleanroom, shown in fig 2.7. This technique lets us write any desired pattern directly onto the substrate and align many layers with calibration markers. Instead of UV light, it employs a 365 nm laser to expose the resist in a printing process. In the project, Draw mode was used at dosage of 250 mJ/cm^2 for large contact areas and 185 mJ/cm^2 for thin contact probes. Each exposure was done twice, to ensure proper exposure. Draw mode works differently that other modes, where it exposes the target area at one go, unlike partwise exposure in other modes. Hence, the actual energy exposed in an area is comparatively low.

2.5 Raman Spectroscopy

Raman spectroscopy is a powerful technique used to probe chemical structure of a sample through light matter interaction. As light interacts with matter, it excites vibrational energy levels, causing energy absorption. After interaction, most of the light is elastically scattered and is termed as Rayleigh scattering while only a small fraction of photons are inelastically scattered owing to vibrational modes of the sample, which corresponds to the vibration energy levels of the molecule. The Raman effect is sensitive to the molecular structure and chemical composition of the material, providing a unique spectral fingerprint for different substances. In case of graphene, there are two principal Raman bands: one at 1580 cm^{-1} , which is called the G band, and the other at 2700 cm^{-1} , which is called the 2D band. These peaks are characteristics of graphene sample and can be identified if a sample shows these peaks. The G peaks correspond to E_{2g} phonons which physically denote inplane vibration of sp^2 carbon atom about its axis. This band is present in all sp^2 carbon systems and provides insights into doping levels. The 2D peak corresponds to the out of plane vibrations of the carbon atoms which is layer and incident laser energy dependent. It is caused through double resonance where two phonons from the transverse optical (TO) phonon branch near the K point of the Brillouin zone interact coherently. In other words, first, an incident photon excites an electron from the valence band. This electron then interacts with a phonon, scattering within the conduction band to another point in the Brillouin zone. Finally, the electron interacts with a second phonon and recombines with a hole, emitting a photon with a different energy than the incident photon and the whole process is called double resonance. In single-layer graphene, the 2D band is sharp and intense due to the constructive interference of the electronic states involved in the double resonance process. In multilayer graphene,

the presence of additional layers modifies the scattering efficiency, which can result in changes in the 2D band intensity.

Experimental Conditions

A 532nm laser was used to probe the sample for Raman analysis. Monolayer flakes after exfoliation and bulk samples were studied through Raman spectroscopy. The samples were placed onto the stage and monolayers were identified through optical microscope followed by optical focusing using 50x lens to obtain sharp image of flakes. The laser intensity was set at 25% (50% for $NbSe_2$) with 1800 grating, acquisition time of 10 secs, accumulation of 5 and RTD time of 2secs. A spectrum near 520 cm^{-1} was taken where readings are calibrated to Si substrate that shows peak at 520 cm^{-1}. Several devices were characterised using this method and they showed high purity Raman spectra. The samples studies were done at room temperature without any strains.

2.6 Physical Property Measurement System

The Cryogenic Ltd Physical Property Measurement System (PPMS) is a state of the art, high-precision instrument developed to measure physical properties in a controlled cryogenic environment. The PPMS used in this project is shown in fig 2.8. It runs across a wide temperature range, typically from 1.8 K to 120 K, with liquid helium closed-cycle cryocooler, and features a superconducting magnet capable of producing magnetic fields upto 9 Tesla. The system provides accurate temperature and magnetic field control, as well as exceptional stability and the option of operating in persistent mode to maintain steady fields for extended periods of time. It offers a wide range of physical tests, including electrical transport (resistivity, Hall effect), magnetization (VSM, AC susceptibility), heat capacity, thermal conductivity, and

dielectric measurements.

Figure 2.8: Cryogenic PPMS

The system is designed for efficient operation, reducing helium consumption and allowing for cryogen-free configurations, making it both cost-effective and suited for long-term experiments.

2.7 FE-SEM

The Field Emission Scanning Electron Microscope (FE-SEM) is a device that images a sample surface using a high-energy electron beam and a cold cathode field emitter. The FE-SEM used in this project is shown in fig 2.9. It uses focused electrons beam irradiation on the sample surface that leads to emission of secondary electrons (SE-1, SE-2, etc) that are collected by the detectors. The energy and angle of emission can be used to map the image of the surface. Some original electrons are back scattered in this process. Collecting these electrons gives information about the irradiated surface.

SE-1 electrons are emitted when near the focus point, while higher SE's are emitted away from the focus point of the beam. SE-2 electrons enhance the brightness, but reduce the overall resolution of the image.

Figure 2.9: FE-SEM

A high electric field is used to ionise electrons from a metal. These electrons are concentrated using magnetic field into a tiny beam that scans the sample, producing precise images and spectrum of surface topography, composition, and characteristics. It requires an ultra-high vacuum to eliminate electron scattering, resulting in high-resolution images with increased brightness and stability when compared to traditional SEMs.

Using these fabrication and characterization techniques, in this thesis, we fabricate Graphene and $NbSe_2$ based heterostructures, and use them to study interfacial quantum properties.

Chapter 3

Fabrication and Characterization of Graphene based devices

3.1 Flake identification

The method described in sec 2.1 was used to obtain a PPC stamp with thin flakes on it. After obtaining flakes on the PPC stamp, a photo is taken and the PPC - flake assembly is inverted and brought in close vicinity of the substrate as shown in fig 3.1a.

(a) Bilayer flake on PPC

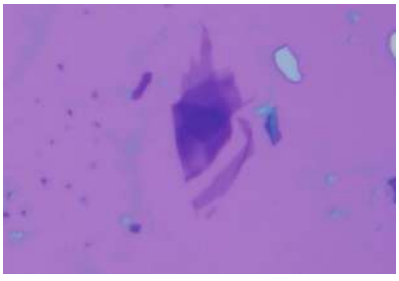

(b) Few layer flakes on SiO_2

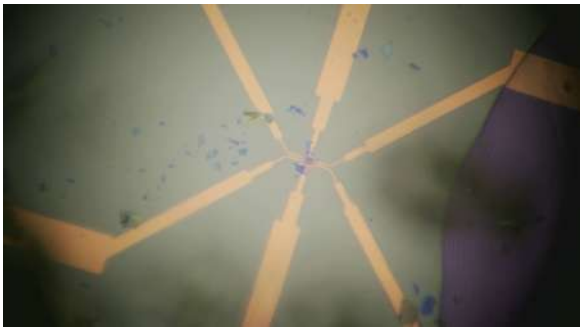

(c) Contrast change

Figure 3.1: Flake identification and transfer

Monolayers are very faintly visible and utmost attention is required to identify monolayers. Thin flakes are visible in the light of wavelength reflected by Si/SiO_2 and can

be used to characterize the number of layers. Contrast study using ImageJ can be used to characterize flake layers. Using the Z movement of the micromanipulator, the flake is made to contact with the substrate as shown in fig 3.1c and a change in contrast is observed. The transfer process is completed after peeling off the PPC at slow rates. The images in fig 3.3 shows the contacts made with different metals in different geometry after graphene is transferred onto the contacts. The samples were then characterized using Raman and contrast study using ImageJ to determine the number of layers [33]. Further, we study quantum transport in the graphene devices made through dry exfoliation.

3.2 Raman and contrast study

Several devices with monolayers and bilayers of graphene were fabricated using dry exfoliation technique. First, the Raman peaks were checked, as shown in fig 3.2 to ensure high quality flakes along with determining the number of layers in the sample as in fig 3.7.

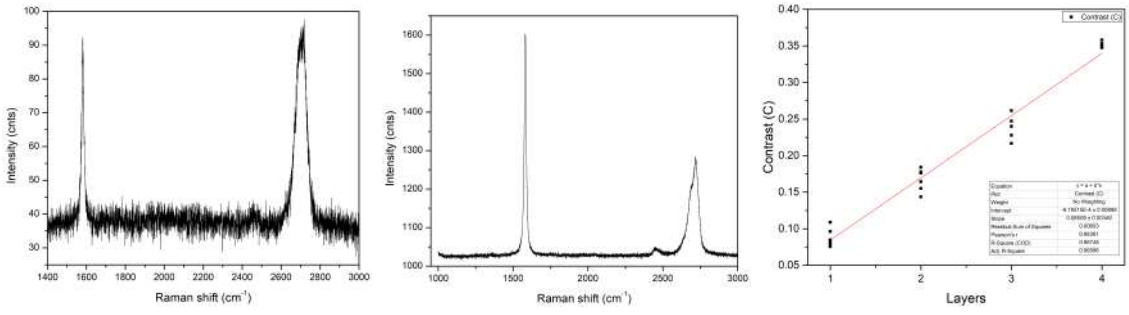

(a) Bilayers (b) Bulk (c) Contrast vs Layers

Figure 3.2: Raman Spectroscopy of thin flakes

The intensity at 2D and G band peaks is given by I_{2D} and I_G respectively. A $\frac{I2D}{I_G}$ $\geq$2 ensures monolayer of graphene on the substrate which can be used for transfer studies. This is logical since G band has no layer effect while intensity of 2D band is

high when graphite is thinned down. The fig 3.2 shows the Raman graph for graphene where, the intensity I_{2D}/I_G is calculated to be ~ 1 indicating a bilayer sample [34]. A bulk sample Raman measurement was taken to ensure defect free and high quality graphene for reference. This sample showed no defect peaks, ensuring graphene used of highest quality. Next the contrast plots were made, where the number of layers had a linear relationship with the optical contrast of the layer. Fig 3.2c shows that each layer adds 0.085 ± 0.03 to the contrast maintaining a linear relationship between contrast and number of layers and it can be used to characterize the number of layers without the Raman spectroscopy.

3.3 Contact Printing and Transport

Two different methods, namely pre patterned and post patterned approach were adopted to fabricate heterostructures. Pre pattern technique utilizes pre patterned electrodes printed onto the substrates prior to exfoliation and the flake is accurately placed onto these electrodes. Two such fabricated devices are shown in fig 3.3.

(a) Pre patterned Ti contacts (b) Pre patterned Gold contacts

Figure 3.3: Placing flakes on contacts

Pre patterning is an easier method for sample fabrication, while minimizing the defects in the contact printing steps. Alas, these electrodes are not suitable for characterization of transport properties of thin flakes, owing to their rough edges due to liftoff.

As shown in fig 3.4a, which is a FE-SEM of a pre patterned flake, we could observe rough tall edges formed due to the acetone lift off and this causes flakes to hang or form uneven contacts, leading to exceptionally high contact resistance with unclear transport properties. This can be observed in fig 3.5, where no as such coherent character was observed in well studied Graphene.

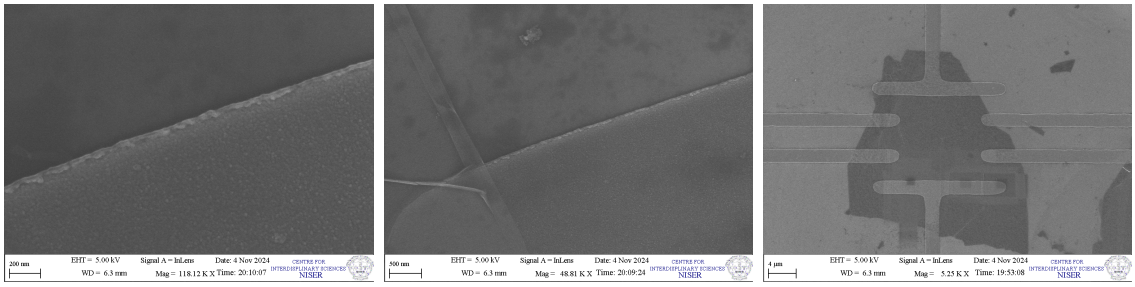

(a) Ridge at corners (b) Uneven contact (c) Device

Figure 3.4: FE-SEM of devices

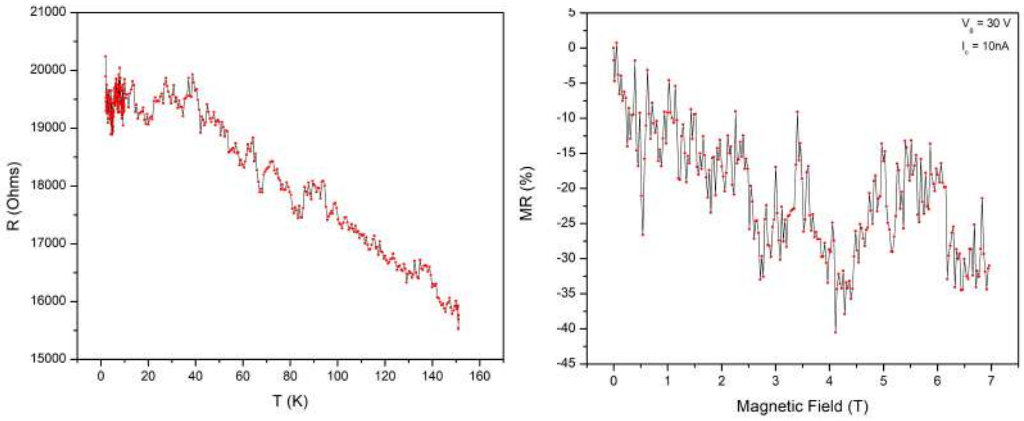

(a) RT (b) MR

Figure 3.5: Transport in Ti electrodes, issues in contacts

Following this, post patterned technique was utilized in further device fabrication. Despite introducing doping in the system, using the post patterned scheme, we successfully fabricated ballistic transport devices that are apt for research. Fig 3.6 shows various devices fabricated using the post patterned scheme. On probing these devices

using transport measurements, proper graphene characteristics were observed which ensured good sample fabrication. This can be seen in fig 3.7b.

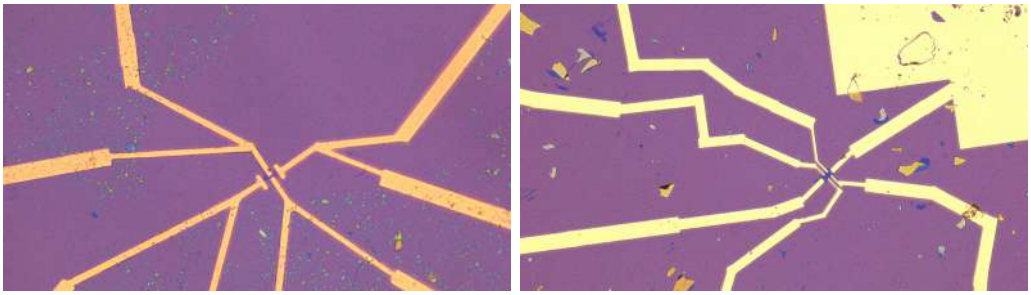

(a) Au/Cr(33/5 nm) (b) Pt contacts with Graphene

Figure 3.6: Post patterned electrodes

The substrate also has an important role in sample purity and and generally, h-BN is first exfoliated on the substrate and the heterostructure is sandwiched between hBN flakes in order to improve the quality of transport [35].

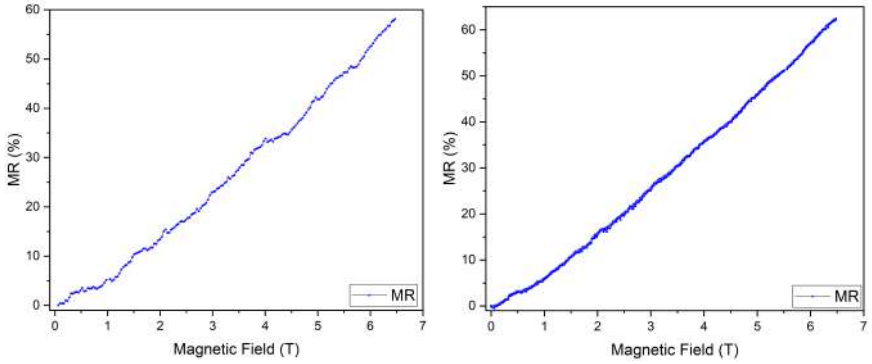

(a) $V_G = 30V$ (b) $V_G = 0$

Figure 3.7: DC Magnetoresistance for bilayer sample with gating

Gating operations were also performed in these samples, whose details are mentioned in sec 3.4. It was essential to understand the effect of gating for higher tunability in quantum systems.

3.4 Electrodes, Contacts and Gating

As mentioned earlier, the doping concentration in Graphene is dependent on the metal used for making contacts. To further understand this, Ti, Nb, Au/Cr and Pt contacts were fabricated onto Graphene devices, as shown in fig 1.3, to study its properties. Further, gating operations had to be implemented to understand this doping concentration. The plots for Au/Cr contacts for a bilayer graphene system is shown in fig 3.8, which shows a good contact with expected MR and Hall resistance measurements. The bias dependent current - gate sweep was not be taken due to burning of the sample, through electrostatic discharge.

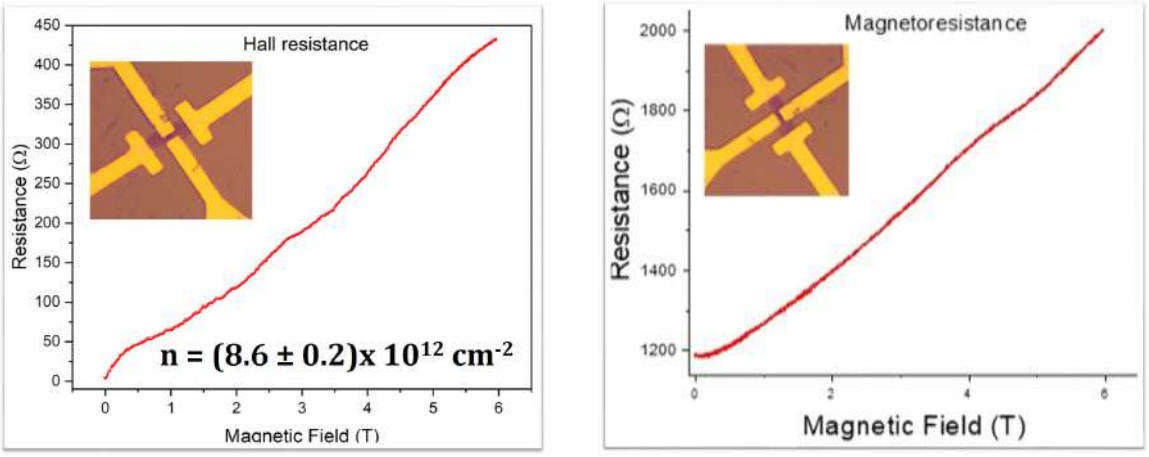

(a) Hall effect (b) Magnetoresistance

Figure 3.8: Transport in Au/Cr electrode bilayer Graphene

Using the Hall resistance formulae 1.3, we obtained the carrier density of the graphene channel and is found to be n= (8.6± 0.2) x 10^{12} cm^{-2}, which matches well with literature, indicating good ballistic transport. Cr/Au (5/30nm) contacts are widely used in literature for making contacts to 2D flakes. Cr acts as an adhesive layer to SiO_2 substrate and Au is used for its high conductivity. Further, the Fermi level of Cr is close to graphene, which is essential for getting an ballistic contact. These

contacts showed the best properties and were used in final device fabrication. Next, to understand the doping and effect of electrodes samples were tested with Pt contacts, which showed good 0V gate properties, but the gating operations were not suitable for these electrodes. The work function of Pt is ($\sim$ 5.5eV), greater than graphene ($\sim$ 4.5eV), thus it p dopes the graphene system. A negative gate bias induces holes in the graphene channel and allow for enhanced conductivity while a positive bias injects electrons in the system, reducing conductivity. The plots for I_d vs V_g for a bias of 10 mV is shown in fig 3.9. This shows that as the gate is increased from negative to positive bias, the resistance increases continuously and takes a sharp increase near the Dirac point, which is expected [36, 37].

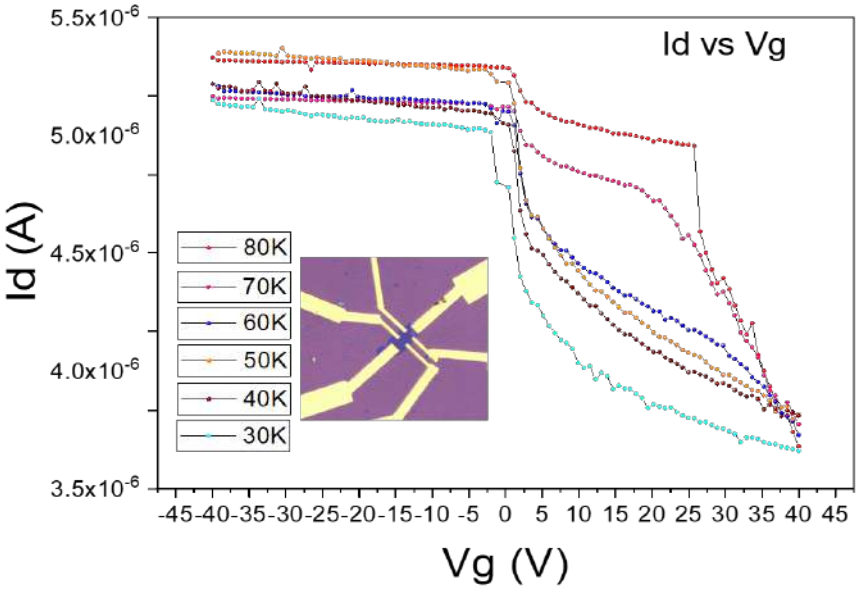

Figure 3.9: I_d vs V_g for Pt contacts on 3L graphene (V_d = 10mV)

Further increasing the gate bias, there is monotonous increase in the sample resistance, which was unexpected, but a sharp second turn at higher bias is observed at higher temperatures, which was even more surprising. This is a signature of Schottky type barrier at the interface, that is modulated through gate bias. We further saw change in concavity of the resistance with bias which is a signature of change

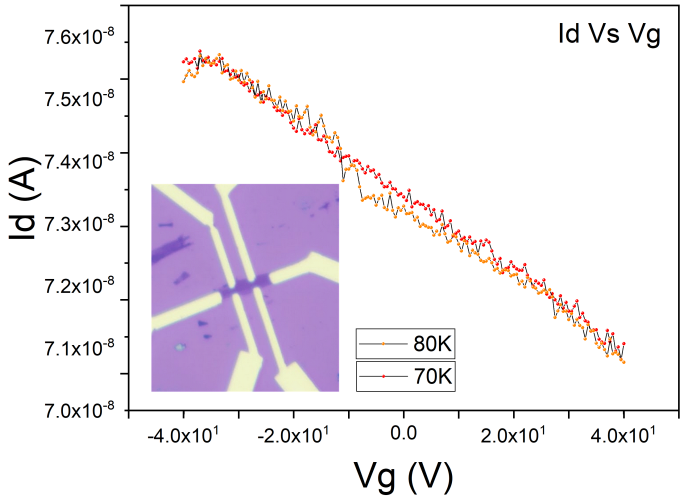

Figure 3.10: I_d vs V_g for Ti contacts on 3L graphene (V_d = 1mV)

in charge carrier, indicating the gating is functional, but not enough for injecting charge carriers for transport. This was observed at higher gate biases at higher temperatures, indicating lower charge injection to the samples as temperature is lowered. Thus, the substrates (p doped) used were not suitable for transport using gating at low temperatures [1].

Next, we used Ti electrodes for gating applications, but were met with a monotonous increase in resistance, without any features, as shown in fig 3.10. This was rather surprising, since we expected a sudden drop in resistance at Dirac point, but it seems the Dirac point was not in the sweep range, due to which we lack any features. This was verified with two different devices, indicating unintentional doping in these systems. Further investigation is required for confirming the doping concentration in this system. We even used different substrates for gating operations, n doped and p doped substrates, but the results were inconclusive, since they showed similar behavior.

3.5 Weak Localization in Graphene

After understanding the proper contacts and gating operations, we wanted to understand effects of superconducting (Nb) contacts to graphene devices. Fig 3.11 shows the transport characteristics of the post patterned (Nb) monolayer devices where RT and near 0T field MR studies were done.

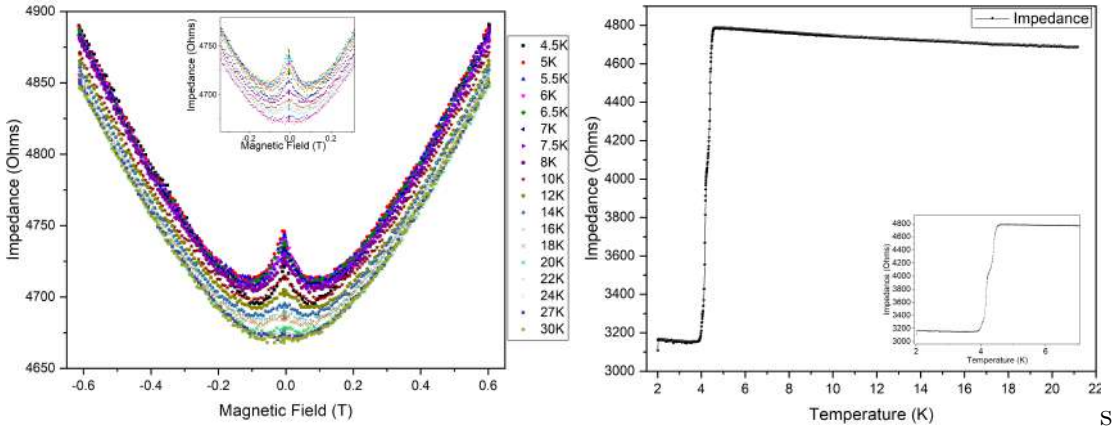

(a) Ridge at corners (b) Uneven contacts

Figure 3.11: RT, RH curve for monolayer sample taken in AC configuration at 20Hz, 100nA bias

The post patterning with Nb helped to obtain lower resistances of the samples along with showing quantum physical phenomena. The MR graph shows a Weak Localisation (WL) effect in the devices caused due to scattering from impurities, forming random paths. In special cases, these random paths form loops in clockwise or anticlockwise directions, introducing a phase to the path trajectories. If the phases match coherently, it causes anti localisation, while incoherence causes weak localisation [38]. Increasing field near zero 0 Tesla leads to negative MR as the back scattering paths have phases including effects from SOC, leading to weak anti locatisation and hence reducing resistance. This is followed by positive MR after a critical value as applying a magnetic field introduces a phase shift in the electron wave functions, disrupting

the constructive interference amplitude of back scattering due breaking of the time-reversal symmetry. The sample showed no WL above 27K. Further RT was done to ensure proper contacts and transport behavior. The electrodes had superconducting transition at 4.2 K, thus we observed a high change in resistance near that temperature and further details can be seen in appendix. In order to see device properties, frequency and current dependent MR were done and yielded same behavior, only changing the overall resistance by constant amounts, indicating no frequency or current dependence of WL upto 1μA currents. As the temperature is increased, the WL effect diminishes due to the reduction of the phase coherence time owing to thermal fluctuations. The WL arises from defects in the samples which are unintentionally introduced at two steps. Firstly, the use of photoresists can cause doping. The other reason is attributed to sputtering that causes defects near the electrodes. These electrodes can also put strain effect in the graphene, changing the density distribution and introducing new effects [39].

Now that we had optimized intermediate steps of graphene device fabrication, we started fabricating devices using $NbSe_2$, a superconductor with a Charge Density Wave order at 33K. These devices hold interesting properties that have many potential applications in quantum technologies.

Chapter 4

Characterization of $NbSe_2$ fabricated devices

We finally fabricated the $NbSe_2$ devices, containing a bulk $NbSe_2$ flake and capped with graphene for protection from environment (oxidation). The intermediate steps were similar to ones followed for graphene device fabrication. The only difference was these samples were spin coated with photoresist as soon as the transfer process was over to avoid sample oxidation. The device photograph in shown in fig 4.1, where the red marked area denotes the Graphene flake and green marked area denotes the $NbSe_2$. The contacts were made using Cr/Au (5/30)nm, with minimal exposure to air and light.

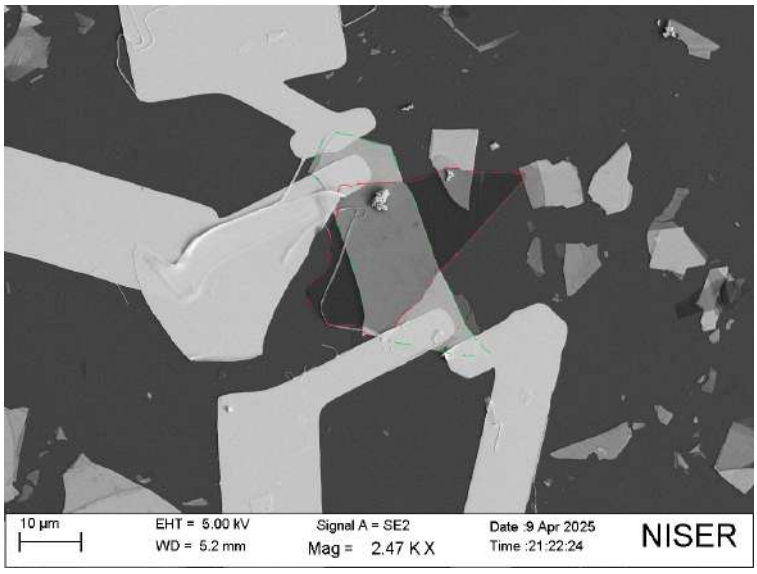

Figure 4.1: SEM image of Capped $NbSe_2$ device

Raman spectroscopy was performed to ensure defect free, $NbSe_2$ flakes, as shown in

fig 4.3. We observed two characteristic peaks A_{1g} and E_{2g} for $NbSe_2$, which confirmed the sample purity. This is rather a bulk sample of $NbSe_2$, as can be confirmed by optical contrast [40]. Nevertheless, it shows the characteristics of $NbSe_2$, which are very interesting. The contacts were made sure to avoid any other underlying flake to prevent film being disconnected from contact pads. This is an essential step, since many samples were wasted due to film coming off, when sputtered over the thick flakes.

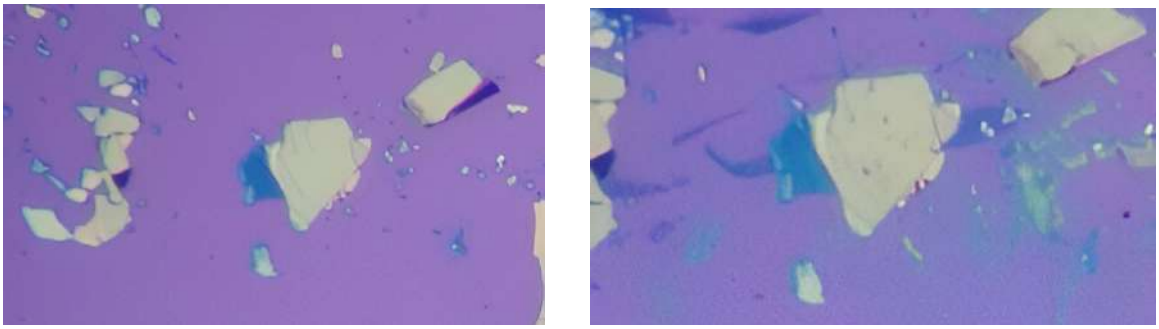

(a) $NbSe_2$ thin flake (b) $NbSe_2$ thin flake capped with Graphene

Figure 4.2: Sample fabrication

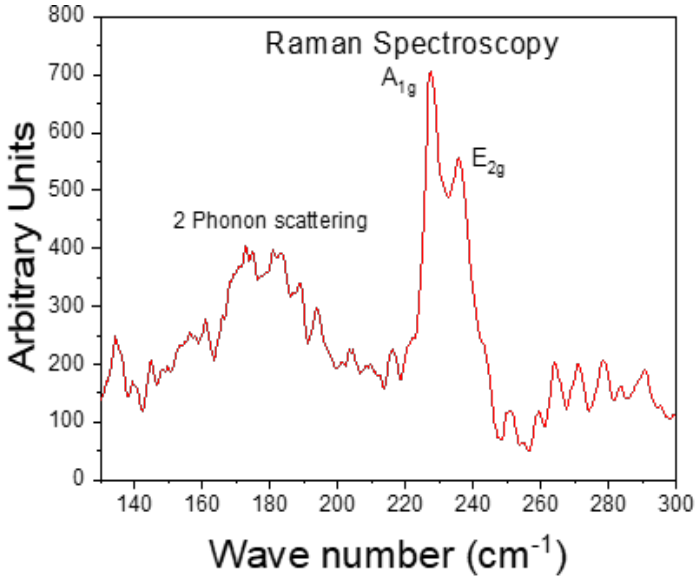

Figure 4.3: Raman Spectroscopy of capped $NbSe_2$ flake

Resistance - temperature measurements with a 4 probe measurement scheme were performed in PPMS with a 1μA DC bias current, which showed a sudden normal - superconducting transition at 6.9 K. Using eq 1.2, the superconducting gap was calculated to be 0.00105eV. This ensured a defect free and thin sample of $NbSe_2$, as shown in fig 4.4a. No secondary transitions were observed, ensuring a single bulk flake without defects. This T_c is slightly lower than the T_c for bulk $NbSe_2$ of 7.2K. Further, a bump in the resistance was observed in RT curve near 33K, which is a signature of CDW transition, shown in fig 4.4b. When the charge lattice reorients, it causes a shift in the atomic lattice, changing the resistance of the sample. We expect this feature to be present till monolayer limit while the T_c shall decrease with thinning of the sample [41]. So, in order to observe these behavior, fabrication of thin layers of $NbSe_2$ for transport is essential.

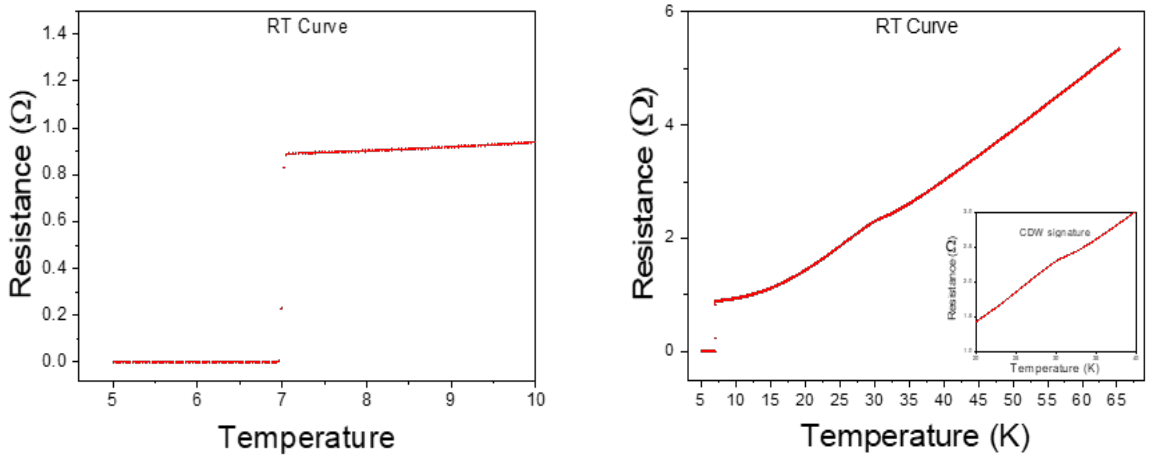

(a) Superconductor - normal state transition (b) CDW

Figure 4.4: Resistance - Temperature graph for capped $NbSe_2$

To further verify superconducting transition, in-plane magnetic field was applied to observe the response of the samples. As expected, increasing the applied magnetic field lowered the superconductor - normal state transition temperature, as shown in

fig 4.5. With higher fields, the sample T_c decreased, along with a slanted transition, instead of a single step transition, which is a characteristic of type 2 superconductors in magnetic field. Due to ising superconductivity, the magnetic field tries to align the spins in particular direction, thus there is a competing order, that reduces the superconducting order parameter. Appying higher fields would result in spin flip transition, killing any superconducting order.

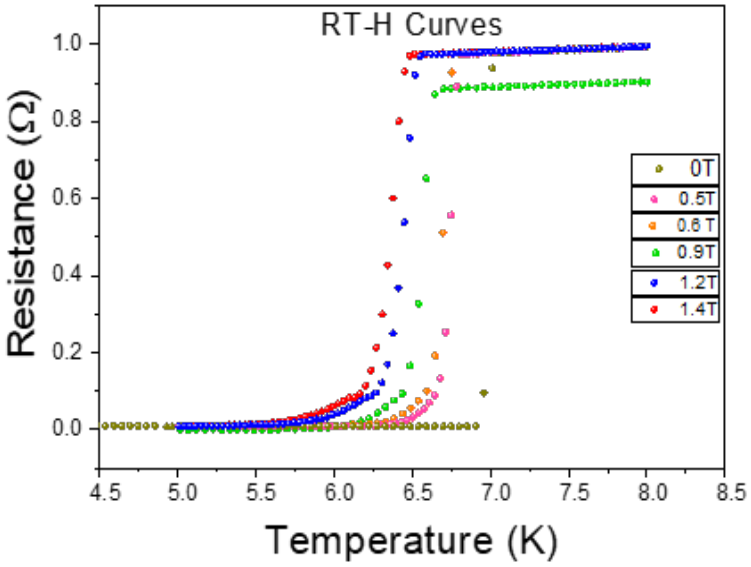

Figure 4.5: RT-H curve for $NbSe_2$

Application of higher fields over the Pauli limit was not possible due to limitations of the PPMS. Finally, no gating was implemented in this device as this was the first working device after several trials of fabrication. Gated devices are delicate to handle due to underlying charge accumulation on the flakes. We fabricated thinner devices for gating operations but could not characterize them due to electrostatic discharge.

4.1 Electrostatic Discharge and Gating

A sample picture of the flake after optimized transfer is shown in fig 4.2a. The small area of the $NbSe_2$ flake connected to the thicker flake was chosen for contact printing

and observing effects of thinning down these superconductors. This was followed by capping by graphene as shown in fig 4.2b. This was finally made into a gated device, but no images were taken before measurement to avoid oxidation of the samples. Often during cooling and sample handling, charge builds up in the samples, that can be harmful to the device. Thus, the samples must be grounded at all times to avoid sample burning. We burnt many samples of graphene and $NbSe_2$ as soon as the ground terminal was connected to the drain electrode due to electrostatic discharge. Due to a large charge accumulation, a huge charge passes through the grounded terminal, causing intense heating and subsequent burning of the sample, even at cryogenic temperatures of the order 10 K. The image of the fabricated burnt device is shown in fig 4.6, which we burnt at 10K.

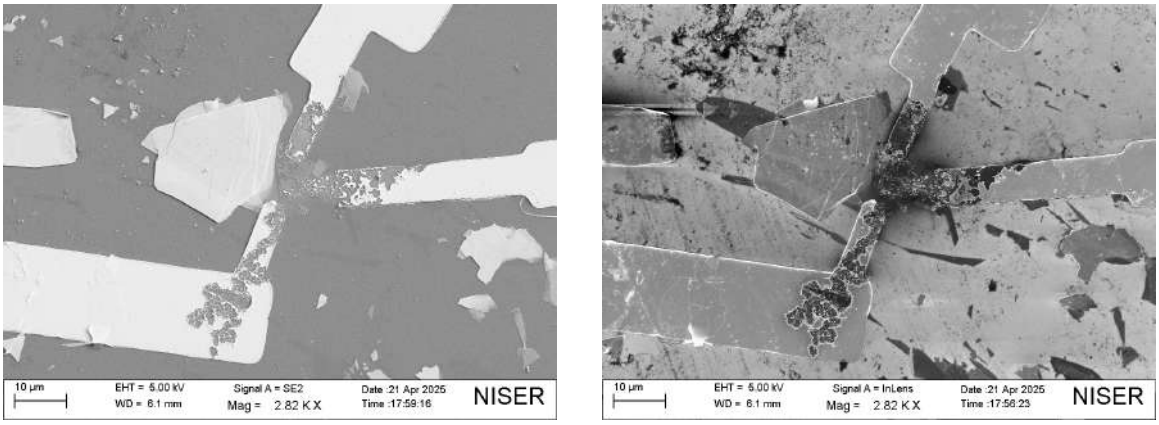

(a) Inlens image of burnt sample

(b) SE2 image of burnt sample

Figure 4.6: Sample damage due to electrostatic discharge

Back gating has been an issue since the start of the experiment, mainly due to issues related to leakage current and discharge, as shown in fig 4.7, where we observed negative current when the bias voltage was negative. Leakage was solved through a sapphire substrate beneath the Si substrate, that reduced leakage by many orders.

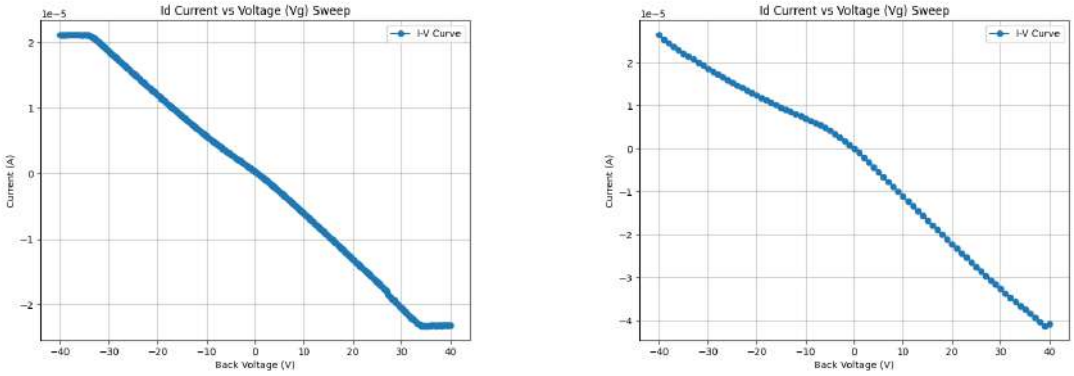

Figure 4.7: Leakage Current

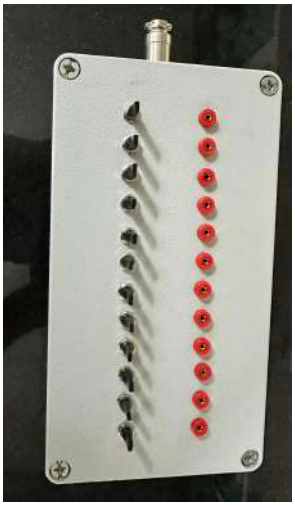

Figure 4.8: Breakout box at lab

This allowed to perform gate dependent measurements with minimal leakage.

The electrostatic discharge can be avoided by using breakout boxes that are always grounded, until the grounding switch is turned off. This ensures any extra charge does not accumulate on the flakes and is sent to the ground directly. We also constructed a breakout box, shown in fig 4.8, with help of NISER electrical workshop, that is being implemented in the PPMS system to reduce sample damage due to discharge.

Summary and Conclusions

In this thesis, we investigated the fundamental properties and emergent behaviors of two-dimensional (2D) materials, with a focus on their distinct structural, electronic, and superconducting characteristics. Beginning with a thorough introduction to the origins and development of 2D materials, we laid the groundwork for understanding the role of reduced dimensionality in modulating material properties.

We studied transition metal dichalcogenides (TMDs), specifically $NbSe_2$, to see how superconductivity manifests in experimentally accessible signatures like resistivity, critical temperature and energy gap. Detailed measurements and analyses of superconductivity in $NbSe_2$ revealed important insights into the interaction between dimensional confinement, charge density wave states, and the onset of superconductivity. Our findings highlight the sensitivity of superconducting transitions to external parameters like temperature and layer number, which is important for designing future quantum devices.

Overall, this work advances our understanding of low-dimensional superconductivity and adds to the larger narrative of 2D materials as key players in next-generation quantum and nanoscale technologies. Future research may focus on coupling mechanisms, interface phenomena, and device integration strategies, bringing us closer to realizing scalable 2D-based superconducting systems.

4.2 Future Directions

Looking ahead, several promising avenues for future research emerge. Despite some fabrication challenges, such as electrical discharge during processing, the $NbSe_2$ devices fabricated thus far are of sufficient high quality to support cutting-edge experimental work. The incorporation of electron beam (E-beam) lithography is a critical next step, as it will allow the fabrication of devices with the sub-micron precision required for studying quantum effects such as the superconducting proximity effect. The ability to consistently produce clean and reproducible van der Waals heterostructures opens the door to fabricating twisted bilayers and heterostructures with controlled rotational alignment. This offers up a productive area in the study of moiré superlattices and emergent correlated phases, including unconventional superconductivity and Mott insulating behavior in systems like twisted bilayer graphene and $NbSe_2$-graphene stacks. These structures act as customizable platforms for probing interactions between flat bands and strong electronic correlations, permitting the discovery of novel quantum ground states.

Beyond fundamental materials physics, the project is ideally positioned to advance to the construction of nanoscale quantum devices such as Josephson junctions, superconducting quantum interference devices (SQUIDs), and field-effect transistors (FETs) based on 2D superconductor. These devices can be combined into basic quantum circuits, allowing for the experimental investigation of superconducting qubits, phase coherence, and quantum transport phenomena. These directions not only describe immediate experimental goals, but also outline a long-term path that has the potential to make substantial contributions to both condensed matter physics and the creation of scalable quantum technology.

Appendix A

4.1 Van Der Waal's forces

The physics behind the cleaving is complex and requires the vertical force to overcome the VdW forces. The VdW forces consists of Keesom, Debye and London forces, which combine to give a power law dependence of the interaction, given by:

$$W(\mathbf{r}) = -\frac{C}{\mathbf{r}^n} \tag{4.1}$$

where $W(\mathbf{r})$ is the interaction potential. For dipole free systems, the interaction potential corresponding to VdW forces have power dependence of 6. Using eq 4.1 and considering two flat surfaces comprising of molecules, we get:

$$W(\mathbf{r}) = -\frac{\pi \mathrm{C}\rho^2}{12D^2} \tag{4.2}$$

In the Hamaker formalism, the corresponding equation becomes:

$$W(\mathbf{r}) = -\frac{A}{12\pi D^2} \tag{4.3}$$

where A $= \pi^2 C_{VdW}\rho_1\rho_2$. where C$_v dW$ measures the VdW force between the two materials surfaces, and ρ_i is their atomic density. Thus, the effective VdW force between the two surfaces per unit area, F_{ad} , is given by:

$$F_{ad} = -\frac{\partial W}{\partial D} = -\frac{A}{6\pi D^3} \tag{4.4}$$

The cohesion energy between two surfaces is determined by their interactions at the equilibrium inter-surface distance. The cohesive force is dependent on the precise

exfoliation pathway and the manner in which the two layers are separated. Eq 4.5 represents the force acting on the layers as they are drawn apart while remaining parallel to one another and perpendicular to the separation distance, represented by (D). When the upper layer peels away from the lower layer over a distance (d), the peeling force density (F_{peel}) can be written as follows:

$$F_{\text{peel}} = \frac{A}{12\pi D^2 d} = F_{\text{ad}} \frac{D}{2d} \tag{4.5}$$

Since the usual interlayer distance D is much lower than any inplane length d, the peeling force F_{peel} is substantially smaller than the adhesion force F_{ad} This condition enables the process of exfoliation.

4.2 BCS Microscopic Framework of superconductivity

The 2nd quantized Hamiltonian for a superconductor is given by:

$$\hat{H}_{\text{BCS}} = \sum_{k,\sigma} \xi_k \, c^\dagger_{k\sigma} c_{k\sigma} \; + \; \sum_{k,k'} V_{kk'} \; c^\dagger_{k\uparrow} c^\dagger_{-k\downarrow} c_{-k'\downarrow} c_{k'\uparrow}. \tag{4.6}$$

Here $\xi_k = \epsilon_k - \mu$ is the single particle energy measured from the chemical potential. The attractive interaction $V_{kk'}$ is typically non-zero only within a Debye shell $|\xi_k|, |\xi_{k'}| < \hbar\omega_D$. The first term typically denotes that the energy kinetic energy and the second term denotes the cooper pairing of spin opposite electrons.

Applying a mean-field decoupling, $\Delta_k = -\sum_{k'} V_{kk'} \langle c_{-k'\downarrow} c_{k'\uparrow} \rangle$, and taking proper approximations, we obtain the following equation:

$$\Delta_k = -\sum_{k'} V_{kk'} \frac{\Delta_{k'}}{2E_{k'}} \tanh \frac{E_{k'}}{2k_B T}, \qquad E_k = \sqrt{\xi_k^2 + |\Delta_k{}^2|}. \tag{4.7}$$

For an s wave, isotropic interaction $V_{kk'} = -V$, the gap becomes momentum-independent, yielding the well known weak coupling solution $\Delta_0 = 1.764\, k_B T_c$ at $T = 0$. The superconducting state is a lower energy state, which can be calculated by subtracting the free energies of the superconducting (F_s) and normal (F_n) states at $T = 0$ gives

$$\Delta F = F_s - F_n = -\frac{1}{2} N(0) \Delta_0^2, \tag{4.8}$$

with $N(0)$ the single spin DOS at the Fermi level. This is the amount of energy lowered due to transition to a superconducting state to normal state.

4.3 Ginzburg–Landau (GL) Theory of Superconductivity

4.3.1 GL Free Energy Functional

We define an order parameter for phase transition in superconductors. Superconducting - Normal state transition is a second order phase transition and the dynamics of this can be captured by the energy functional. Near T_c, expanding the complex order parameter $\psi(r)$ (density of Cooper pairs), we obtain:

$$\mathcal{F}_{\mathrm{GL}} = \int d^3 r \, \left[\alpha |\psi|^2 + \frac{\beta}{2} |\psi|^4 + \frac{1}{2m^*} | -i\hbar \nabla - 2eA|^2 \psi + \frac{B^2}{2\mu_0} \right], \tag{4.9}$$

where $\alpha = \alpha_0 (T - T_c)$ and $\beta > 0$. Minimizing $\mathcal{F}_{\mathrm{GL}}$ with respect to ψ^* and A gives us the first GL equation:

4.3.2 First GL Equation

$$\alpha \psi + \beta |\psi|^2 + \frac{1}{2m^*} (-i\hbar \nabla - 2eA/c)^2 \psi = 0. \tag{4.10}$$

These yield some characteristic length scales, which can be used to characterize the sample nature:

$$\xi = \sqrt{\frac{\hbar^2}{2m^* |\alpha|}}, \quad \lambda = \sqrt{\frac{m^*}{\mu_0 (2e)^2 |\psi_0|^2}}, \qquad \kappa = \frac{\lambda}{\xi},$$

which distinguish type I ($\kappa < 1/\sqrt{2}$) from type II ($\kappa > 1/\sqrt{2}$) superconductors. In order to understand the beghaviour of magnetic field inside the

4.3.3 London Electrodynamics - The second GL equations

Assuming that the magnitude of the superconducting order parameter $|\psi|$ is constant and only the phase varies, the wavefunction can be written as $\psi = \psi_0 e^{i\theta}$. The corresponding supercurrent density is given by

$$\mathbf{J}_s = -\frac{n_s e^2}{m^*}\left(\mathbf{A} + \frac{\Phi_0}{2\pi}\nabla\theta\right),$$

where n_s is the density of superconducting carriers, e is the elementary charge, m^* is the effective mass of the carriers (typically twice the electron mass, $2m_e$, for Cooper pairs), $\mathbf{A}$ is the magnetic vector potential such that $\mathbf{B} = \nabla \times \mathbf{A}$, θ is the phase of the wavefunction, and $\Phi_0 = h/2e$ is the magnetic flux quantum. Taking the curl of the supercurrent equation gives

$$\nabla \times \mathbf{J}_s = -\frac{n_s e^2}{m^*}\nabla \times \mathbf{A} = -\frac{n_s e^2}{m^*}\mathbf{B},$$

which is the second London equation.

4.3.4 London Penetration Depth

From Maxwell's equations in the static limit (neglecting displacement current), we have $\nabla \times \mathbf{B} = \mu_0 \mathbf{J}_s$. To find the dynamics of magnetic field inside type II superconductors, we take the curl of both sides yields:

$$\nabla \times (\nabla \times \mathbf{B}) = \mu_0 \nabla \times \mathbf{J}_s.$$

Using the vector identity $\nabla \times (\nabla \times \mathbf{B}) = \nabla(\nabla \cdot \mathbf{B}) - \nabla^2 \mathbf{B}$, and noting that $\nabla \cdot \mathbf{B} = 0$, we find

$$-\nabla^2 \mathbf{B} = \mu_0 \left(-\frac{n_s e^2}{m^*}\mathbf{B}\right),$$

which simplifies to

$$\nabla^2 \mathbf{B} = \frac{1}{\lambda^2}\mathbf{B},$$

where λ is the London penetration depth, defined by

$$\lambda = \sqrt{\frac{m^*}{\mu_0 n_s e^2}}.$$

This differential equation describes the exponential decay of the magnetic field inside a superconductor. For a one-dimensional geometry (e.g., magnetic field entering the surface along the x-direction), the solution is

$$B(x) = B_0 e^{-x/\lambda},$$

where B_0 is the field at the surface. This result describes the Meissner effect, in which magnetic fields are expelled from the interior of a superconductor and decay exponentially with characteristic length scale λ [42].

References

[1] Ferney A. Chaves, David Jimenez, Aron W. Cummings, and Stephan Roche. Physical model of the contact resistivity of metal-graphene junctions. *Journal of Applied Physics*, 115(16), April 2014.

[2] Shatha Mahdi. *Synthesis and study the structural, electrical and mechanical properties of polymer composite superconductor*. PhD thesis, 06 2018.

[3] A. K. Geim and K. S. Novoselov. The rise of graphene. *Nature Materials*, 6(3):183–191, March 2007.

[4] Yu Long, Ying Tao, Wei Lv, and Quan-Hong Yang. Making 2d materials sparkle in energy storage via assembly. *Accounts of Chemical Research*, 57(18):2689–2699, August 2024.

[5] Kin Fai Mak and Jie Shan. Photonics and optoelectronics of 2d semiconductor transition metal dichalcogenides. *Nature Photonics*, 10(4):216–226, March 2016.

[6] Dehui Deng, K. S. Novoselov, Qiang Fu, Nanfeng Zheng, Zhongqun Tian, and Xinhe Bao. Catalysis with two-dimensional materials and their heterostructures. *Nature Nanotechnology*, 11(3):218–230, March 2016.

[7] K. S. Novoselov, A. Mishchenko, A. Carvalho, and A. H. Castro Neto. 2d materials and van der waals heterostructures. *Science*, 353(6298), July 2016.

[8] Joseph G Checkelsky, B Andrei Bernevig, Piers Coleman, Qimiao Si, and Silke Paschen. Flat bands, strange metals and the kondo effect. *Nat. Rev. Mater.*, 9(7):509–526, February 2024.

[9] M. Kögl, P. Soubelet, M. Brotons-Gisbert, A. V. Stier, B. D. Gerardot, and J. J. Finley. Moire straintronics: a universal platform for reconfigurable quantum materials. *npj 2D Materials and Applications*, 7(1), April 2023.

[10] Yu-Chuan Lin, Riccardo Torsi, Rehan Younas, Christopher L. Hinkle, Albert F. Rigosi, Heather M. Hill, Kunyan Zhang, Shengxi Huang, Christopher E. Shuck, Chen Chen, Yu-Hsiu Lin, Daniel Maldonado-Lopez, Jose L. Mendoza-Cortes, John Ferrier, Swastik Kar, Nadire Nayir, Siavash Rajabpour, Adri C. T. van Duin, Xiwen Liu, Deep Jariwala, Jie Jiang, Jian Shi, Wouter Mortelmans, Rafael Jaramillo, Joao Marcelo J. Lopes, Roman Engel-Herbert, Anthony Trofe, Tetyana Ignatova, Seng Huat Lee, Zhiqiang Mao, Leticia Damian, Yuanxi Wang, Megan A. Steves, Kenneth L. Knappenberger, Zhengtianye Wang, Stephanie Law, George Bepete, Da Zhou, Jiang-Xiazi Lin, Mathias S. Scheurer, Jia Li, Pengjie Wang, Guo Yu, Sanfeng Wu, Deji Akinwande, Joan M. Redwing, Mauricio Terrones, and Joshua A. Robinson. Recent advances in 2d material theory, synthesis, properties, and applications. *ACS Nano*, 17(11), May 2023.

[11] *Nature Electronics*, 7(8):621–621, August 2024.

[12] Xiao Tang and Liangzhi Kou. 2d janus transition metal dichalcogenides: Properties and applications. *physica status solidi (b)*, 259(4), January 2022.

[13] Artur Branny, Santosh Kumar, Raphael Proux, and Brian D Gerardot. Deterministic strain-induced arrays of quantum emitters in a two-dimensional semiconductor. *Nature Communications*, 8(1), May 2017.

[14] Arne Quellmalz. *Integration of Two-Dimensional Materials for Electronics and Photonics*. PhD thesis, KTH Royal Institute of Technology, Stockholm, Sweden, 2022.

[15] Yuan Cao, Valla Fatemi, Shiang Fang, Kenji Watanabe, Takashi Taniguchi, Efthimios Kaxiras, and Pablo Jarillo-Herrero. Unconventional superconductivity in magic-angle graphene superlattices. *Nature*, 556(7699):43,250, March 2018.

[16] Luzhao Sun, Guowen Yuan, Libo Gao, Jieun Yang, Manish Chhowalla, Meysam Heydari Gharahcheshmeh, Karen K. Gleason, Yong Seok Choi, Byung Hee Hong, and Zhongfan Liu. Chemical vapour deposition. *Nature Reviews Methods Primers*, 1(1), January 2021.

[17] K. S. Novoselov, Z. Jiang, Y. Zhang, S. V. Morozov, H. L. Stormer, U. Zeitler, J. C. Maan, G. S. Boebinger, P. Kim, and A. K. Geim. Room-temperature quantum hall effect in graphene. *Science*, 315(5817):1379, March 2007.

[18] Teresa Cusati, Gianluca Fiori, Amit Gahoi, Vikram Passi, Max C. Lemme, Alessandro Fortunelli, and Giuseppe Iannaccone. Electrical properties of graphene-metal contacts. *Scientific Reports*, 7(1), July 2017.

[19] Enze Zhang, Xian Xu, Yi-Chao Zou, Linfeng Ai, Xiang Dong, Ce Huang, Pengliang Leng, Shanshan Liu, Yuda Zhang, Zehao Jia, Xinyue Peng, Minhao Zhao, Yunkun Yang, Zihan Li, Hangwen Guo, Sarah J. Haigh, Naoto Nagaosa, Jian Shen, and Faxian Xiu. Nonreciprocal superconducting nbse2 antenna. *Nature Communications*, 11(1), November 2020.

[20] Sunny Gupta, Wenjing Wu, Shengxi Huang, and Boris I. Yakobson. Single-photon emission from two-dimensional materials, to a brighter future. *The Journal of Physical Chemistry Letters*, 14(13):3274, March 2023.

[21] Antonio Barone and Gianfranco Paterno. *Physics and Applications of the Josephson Effect*. Wiley, July 1982.

[22] Michael Tinkham and Victor Emery. Introduction to superconductivity. *Physics Today*, 49(10):74, October 1996.

[23] Werner Buckel and Reinhold Kleiner. *Superconductivity: Fundamentals and Applications*. Wiley, January 2004.

[24] Belqees Hassan. *Superconducting Devices: From Quantum Computing to Energy Transmission*. IntechOpen, December 2024.

[25] Alex Hamill, Brett Heischmidt, Egon Sohn, Daniel Shaffer, Kan-Ting Tsai, Xi Zhang, Xiaoxiang Xi, Alexey Suslov, Helmuth Berger, Laszlo Forro, Fiona J. Burnell, Jie Shan, Kin Fai Mak, Rafael M. Fernandes, Ke Wang, and Vlad S. Pribiag. Two-fold symmetric superconductivity in few-layer nbse2. *Nature Physics*, 17(8):954, April 2021.

[26] Tianhui Zhu, Peter M. Litwin, Md. Golam Rosul, Devin Jessup, Md. Sabbir Akhanda, Farjana F. Tonni, Sergiy Krylyuk, Albert V. Davydov, Petra Reinke, Stephen J. McDonnell, and Mona Zebarjadi. Transport properties of few-layer nbse2: From electronic structure to thermoelectric properties. *Materials Today Physics*, 27:100789, October 2022.

[27] Xiaoxiang Xi, Zefang Wang, Weiwei Zhao, Ju-Hyun Park, Kam Tuen Law, Helmuth Berger, Laszlo Forro, Jie Shan, and Kin Fai Mak. Ising pairing in superconducting nbse2 atomic layers. *Nature Physics*, 12(2):139–143, November 2015.

[28] Asish K. Kundu, Anil Rajapitamahuni, Elio Vescovo, Ilya I. Klimovskikh, Helmuth Berger, and Tonica Valla. Charge density waves and the effects of uniaxial strain on the electronic structure of 2h-nbse2. *Communications Materials*, 5(1), October 2024.

[29] Paul Dreher, Wen Wan, Alla Chikina, Marco Bianchi, Haojie Guo, Rishav Harsh, Samuel Manas-Valero, Eugenio Coronado, Antonio J. Martinez-Galera, Philip Hofmann, Jill A. Miwa, and Miguel M. Ugeda. Proximity effects on the charge density wave order and superconductivity in single-layer nbse2. *ACS Nano*, 15(12):19430–19438, November 2021.

[30] Hidetoshi Fukuyama, Hiromichi Ebisawa, and Yasushi Wada. Theory of hall effect. i: Nearly free electron. *Progress of Theoretical Physics*, 42(3):494–511, September 1969.

[31] Z. Jiang, Y. Zhang, Y.-W. Tan, H.L. Stormer, and P. Kim. Quantum hall effect in graphene. *Solid State Communications*, 143(2):14–19, July 2007.

[32] Philipus N. Hishimone, Hiroki Nagai, and Mitsunobu Sato. *Methods of Fabricating Thin Films for Energy Materials and Devices*. IntechOpen, July 2020.

[33] Katumo Ngei Benjamin Mbaluka John Paul Kimeu Ngumbi. Determination of graphene layers by optical imaging contrast analysis. *International Journal of Innovative Research in Science, Engineering and Technology*, 4:10459–10469, 11 2015.

[34] Van Tu Nguyen, Huu Doan Le, Van Chuc Nguyen, Thi Thanh Tam Ngo, Dinh Quang Le, Xuan Nghia Nguyen, and Ngoc Minh Phan. Synthesis of multilayer graphene films on copper tape by atmospheric pressure chemical vapor deposition method. *Advances in Natural Sciences: Nanoscience and Nanotechnology*, 4:035012, 6 2013.

[35] Leonardo Martini, Vaidotas Miseikis, David Esteban, Jon Azpeitia, Sergio Pezzini, Paolo Paletti, Michal W. Ochapski, Domenica Convertino, Mar Garcia Hernandez, Ignacio Jimenez, and Camilla Coletti. Scalable high-mobility

graphene/hbn heterostructures. *ACS Applied Materials amp; Interfaces*, 15(31):37794, July 2023.

[36] Fengnian Xia, Vasili Perebeinos, Yu-ming Lin, Yanqing Wu, and Phaedon Avouris. The origins and limits of metal and graphene junction resistance. *Nature Nanotechnology*, 6(3):179, February 2011.

[37] Matthias Konig, Gunther Ruhl, Amit Gahoi, Sebastian Wittmann, Tobias Preis, Joerg-Martin Batke, Ioan Costina, and Max C. Lemme. Accurate graphene-metal junction characterization. *IEEE Journal of the Electron Devices Society*, 7:219, 2019.

[38] R. V. Gorbachev, F. V. Tikhonenko, A. S. Mayorov, D. W. Horsell, and A. K. Savchenko. Weak localization in bilayer graphene. *Physical Review Letters*, 98:176805, 4 2007.

[39] F. V. Tikhonenko, D. W. Horsell, R. V. Gorbachev, and A. K. Savchenko. Weak localization in graphene flakes. *Physical Review Letters*, 100:056802, 2 2008.

[40] Hong Wang, Xiangwei Huang, Junhao Lin, Jian Cui, Yu Chen, Chao Zhu, Fucai Liu, Qingsheng Zeng, Jiadong Zhou, Peng Yu, Xuewen Wang, Haiyong He, Siu Hon Tsang, Weibo Gao, Kazu Suenaga, Fengcai Ma, Changli Yang, Li Lu, Ting Yu, Edwin Hang Tong Teo, Guangtong Liu, and Zheng Liu. High-quality monolayer superconductor nbse2 grown by chemical vapour deposition. *Nature Communications*, 8(1), August 2017.

[41] Adel Nader and Pierre Monceau. Critical field of 2h-nbse2 down to 50mk. *SpringerPlus*, 3:16, 01 2014.

[42] M. R. Beasley. Notes on the ginzburg-landau theory. ICMR Summer School on Novel Superconductors, University of California, Santa Barbara, August 2009.